# MEASURING THE MEAN AND SCATTER OF THE X-RAY LUMINOSITY – OPTICAL RICHNESS RELATION FOR MAXBCG GALAXY CLUSTERS

E. S. Rykoff[1,2], T. A. McKay[2,3,4], M. A. Becker[2], A. Evrard[2,3,4], D. E. Johnston[5], B. P. Koester[6], E. Rozo[7], E. S. Sheldon[8], R. H. Wechsler[9]

*Draft version September 11, 2007*

## ABSTRACT

Determining the scaling relations between galaxy cluster observables requires large samples of uniformly observed clusters. We measure the mean X-ray luminosity–optical richness ($\bar{L}_X - \bar{N}_{200}$) relation for an approximately volume-limited sample of more than 17,000 optically-selected clusters from the maxBCG catalog spanning the redshift range $0.1 < z < 0.3$. By stacking the X-ray emission from many clusters using *ROSAT* All-Sky Survey data, we are able to measure mean X-ray luminosities to $\sim 10\%$ for clusters in nine independent optical richness bins. In addition, we are able to crudely measure individual X-ray emission from $\sim 800$ of the richest clusters. Assuming a log-normal form for the scatter in the $L_X - N_{200}$ relation, we measure $\sigma_{\ln L} = 0.86 \pm 0.03$ at fixed $N_{200}$. This scatter is large enough to significantly bias the mean stacked relation. The corrected median relation can be parameterized by $\widetilde{L}_X = e^\alpha (\bar{N}_{200}/40)^\beta \, 10^{42} \, h^{-2} \, \mathrm{ergs\,s^{-1}}$, where $\alpha = 3.57 \pm 0.08$ and $\beta = 1.82 \pm 0.05$. We find that X-ray selected clusters are significantly brighter than optically-selected clusters at a given optical richness. This selection bias explains the apparently X-ray underluminous nature of optically-selected cluster catalogs.

*Subject headings:* galaxies: clusters – X-rays: galaxies: clusters

## 1. INTRODUCTION

Galaxy clusters, as the largest peaks in the cosmic density field, play an important role in astrophysics and cosmology (e.g. Borgani 2003; Voit 2005). Structure formation theory, realized in large scale N-body simulations, makes robust predictions for cluster space density and clustering within various cosmological models. Since clusters are also the most observationally accessible features of large scale structure, they provide an opportunity to place strong constraints on both cosmological parameters and the growth of structure. The great challenge of cluster cosmology lies in confidently relating the dark matter halos we can robustly predict to the baryonic structures we observe. Substantial work is being done to close the gap between theory and observations from both sides.

On the theory side, numerical simulations of ever increasing complexity and resolution provide new insights into the evolution of baryons within clusters, and to elucidate the connection between cluster galaxies and dark matter substructure (Nagai & Kravtsov 2005; Conroy et al. 2006). Observationally, much work is being done to assemble large samples of clusters detected and observed in a wide variety of ways. This is possible because galaxy clusters provide a rich suite of observables. Optical light is emitted by individual cluster galaxies as well as intracluster stars. X-rays are emitted by both the hot intracluster medium (ICM) and AGN within cluster galaxies. This same hot ICM scatters microwave background photons passing through the cluster, distorting their spectrum. Finally, the total projected mass distribution of the cluster produces weak and sometimes strong lensing distortions in the images of background galaxies. Each of these observables presents an opportunity to detect clusters and measure their properties. When combined, they allow us to cross-check our understanding of cluster physics in a variety of ways.

Clusters were first detected as early as the 18th century as anomalous groupings of similarly bright galaxies (Biviano 2000). Optical surveys, which are relatively inexpensive, have long provided the largest cluster catalogs, primarily because of their ability to detect objects with relatively low mass thresholds. While successful in identifying thousands of clusters (Abell 1958; Abell et al. 1989) and providing the first evidence for dark matter (Zwicky 1933, 1937), early optical detection was plagued by projection of galaxies along the line of sight (Collins et al. 1995). Precise CCD photometry has enabled searches for galaxies clustered in space, brightness, and color (for a review of optical selection, see Gal 2006), substantially reducing the problems of projection. These more recent optical surveys also naturally provide accurate photometric redshifts.

With the advent of X-ray satellites, detection of thermal emission from the hot ICM became possible (Gursky et al. 1971). Because X-ray emission depends on the

[1] TOBASGO Fellow, Physics Department, University of California at Santa Barbara, 3019 Broida Hall, Santa Barbara, CA 93106, erykoff@physics.ucsb.edu
[2] Physics Department, University of Michigan, Ann Arbor, MI 48109
[3] Astronomy Department, University of Michigan, Ann Arbor, MI 48109
[4] Michigan Center for Theoretical Physics, Ann Arbor, MI 48109
[5] Jet Propulsion Laboratory, 4800 Oak Grove Drive, Pasadena, CA 91109
[6] Department of Astronomy, The University of Chicago, Chicago, IL 60637
[7] CCAPP Fellow, The Ohio State University, Columbus, OH 43201
[8] Center for Cosmology and Particle Physics, Physics Department, New York University, New York, NY 10003
[9] Kavli Institute for Particle Astrophysics and Cosmology, Physics Department and Stanford Linear Accelerator Center, Stanford University, 382 Pueblo Mall, Stanford, CA 94305

square of the density, this provides a higher contrast that is largely immune to projection effects. But when spatial resolution is low, contamination from non-thermal X-ray sources can be a difficult problem. These can be point sources like AGN, the non-thermal emission from a cooling core, or ongoing merger activity that has thrown a cluster out of thermal equilibrium. Over the last several decades, X-ray surveys have been used to assemble a large number of cluster catalogs (Gioia & Luppino 1994; Ebeling et al. 1996; Rosati et al. 1998; Romer et al. 2000; Böhringer et al. 2000; Mullis et al. 2003; Böhringer et al. 2004; Burenin et al. 2006). Much of our understanding of cluster physics today derives from these X-ray selected catalogs.

Substantial effort has gone into comparing optically and X-ray selected catalogs (Bahcall 1977; Edge & Stewart 1991; Donahue et al. 2001, 2002; Mulchaey et al. 2003; Yee & Ellingson 2003; Gilbank et al. 2004; Popesso et al. 2004), and to comparing optical and X-ray properties of clusters to their weak lensing and SZ signals (Squires et al. 1996; Allen 1998; Fischer 1999; Zaroubi et al. 2001; Dahle et al. 2002; Cypriano et al. 2004; De Filippis et al. 2005; Mahdavi et al. 2005; LaRoque et al. 2006; Hoekstra 2007; Mahdavi et al. 2007; Bardeau et al. 2007). Comprehensive comparisons of optical and X-ray properties of clusters have been hampered by the lack of large samples that are uniformly observed in both passbands.

In this paper we describe measurements of the X-ray properties of the largest publicly available optically-selected cluster sample: the maxBCG catalog (Koester et al. 2007a). This approximately volume-limited cluster catalog spans the redshift range from $0.1 < z < 0.3$. Uniform optical photometry and relatively precise photometric redshifts ($\Delta_z \leq 0.015$) for all these clusters are available from the same Sloan Digital Sky Survey (SDSS: York et al. 2000) data from which the clusters were selected. X-ray observations of all these maxBCG clusters are available from the *ROSAT* All-Sky Survey (RASS: Voges et al. 1999). While RASS exposures are too shallow to allow significant individual detections of every maxBCG cluster, they provide precise measurements of the mean X-ray luminosity ($\bar{L}_X$) as a function of optical richness and redshift. In addition, the low signal-to-noise measurements of X-ray emission from individual clusters can be used both to confirm the measurement of mean X-ray emission obtained by stacking and to provide estimates of the scatter in the optical richness–X-ray luminosity relation.

The maxBCG catalog has been studied in a variety of complementary ways. For example, both dynamical (Becker et al. 2007, henceforth B07) and weak lensing (Sheldon et al. 2007; Johnston et al. 2007, S07, J07) observations of these clusters have been extracted from SDSS data. These earlier observations can be combined with the mean $\bar{L}_X$ measurements presented here to provide further insight into cluster physics. The $\bar{L}_X$–$\sigma$ relation inferred for maxBCG clusters is described here, while the corresponding $\bar{L}_X$–$M_{200}$ relation obtained from weak lensing is discussed in a companion letter (Rykoff et al. 2007).

An analysis similar to that reported in this paper was performed for the NIR selected 2MASS cluster catalog by Dai, Kochanek, & Morgan (2007, henceforth DKM07). The 2MASS NIR flux-limited catalog has ∼ 4000 nearby

($\bar{z} \sim 0.02$) groups and clusters ranging in mass from $\sim 10^{13} - 10^{15} \, M_\odot$, selected with a matched-filter algorithm (Kochanek et al. 2003). DKM07 are the first to take a large optically-selected cluster catalog and measure the mean (stacked) X-ray properties using RASS, rather than simply cross-correlating optically-selected and X-ray-selected clusters. They find that the X-ray luminosity of 2MASS clusters scales with optical richness (their $N_{*666}$, the number of galaxies brighter than $L_*$ within $\sim R_{200}$). In addition, they derive X-ray temperatures and hydrostatic masses for the stacked 2MASS clusters.

In Section 2, we briefly review the SDSS data, maxBCG catalog, and RASS data on which this study is based. Section 3 describes our measurement of X-ray luminosities for individual clusters, as well as our methods for determining the mean X-ray luminosity of a set of clusters with similar richness. We describe the mean relation of X-ray luminosity as a function of richness, scatter in this relation, and the underlying median $\widetilde{L}_X - \bar{N}_{200}$ relation in Section 4. Section 5 discusses several possible sources of systematic bias in these results. In Section 6 we combine these results with dynamical measurements of maxBCG clusters to produce a measurement of the $\widetilde{L}_X - \widetilde{\sigma}$ relation. Conclusions and some discussion of future work are presented in Section 7. Throughout this work we use a $\Lambda$CDM cosmology with $H_0 = 100 \, h \, \mathrm{km \, s^{-1}}$ and $\Omega_m = 1 - \Omega_\Lambda = 0.3$.

## 2. INPUT DATA

The measurements described here are based on two wide-area imaging surveys; SDSS and RASS. Galaxy clusters are selected from the SDSS five-band imaging data using a red sequence selection method. SDSS data also allow measurement of cluster redshifts and richnesses. X-ray emission from these clusters is then measured by from the RASS photon maps. In this section we describe briefly the SDSS imaging data, galaxy cluster selection and calibration, and RASS input data.

### 2.1. *SDSS data*

Optical data for this study are drawn from Sloan Digital Sky Survey[10]: a combined imaging and spectroscopic survey of $10^4$ deg$^2$ in the North Galactic Cap and a smaller region in the South. The imaging survey was carried out in drift-scan mode in five SDSS filters ($u$, $g$, $r$, $i$, $z$) to a limiting magnitude of $r < 22.5$ (Fukugita et al. 1996; Gunn et al. 1998; Smith et al. 2002). Photometric errors are typically limited at bright magnitudes by systematic uncertainties at the 3% level. The spectroscopic survey targets both a "main" sample of galaxies with $r < 17.8$ and a median redshift of $z \sim 0.1$ (Strauss et al. 2002) and a "luminous red galaxy" sample (Eisenstein et al. 2001) which is approximately volume limited out to z=0.38. For more details of the SDSS see York et al. (2000) and Adelman-McCarthy & et al. (2007).

### 2.2. *maxBCG Catalog*

The maxBCG cluster catalog is selected from imaging data contained in DR5 of the SDSS. Selection of galaxy clusters from this imaging data is done using the

---

[10] http://www.sdss.org

"maxBCG" algorithm. Details of the algorithm are presented in Koester et al. (2007b), while the catalog and a description of its properties may be found in Koester et al. (2007a). In brief, the algorithm exploits two well-known features of rich galaxy clusters in addition to the tight spatial clustering of cluster galaxies. First, the bright end of the cluster luminosity function is dominated by red sequence galaxies with a small dispersion in color-magnitude space (the E/S0 ridgeline). Second, clusters contain a distinct brightest cluster galaxy (BCG) located near the center of the galaxy distribution. While some clusters lack an obvious central, dominant galaxy, every cluster does possess some red sequence galaxy brighter than any other.

The algorithm measures independently the likelihood that a galaxy is spatially located in an overdensity of E/S0 ridgeline galaxies with similar $g - r$ and $r - i$ colors, and that it has the color and magnitude properties of a typical BCG. Both likelihoods are evaluated for every SDSS galaxy at a grid of redshifts. The redshift which maximizes the product of these likelihoods is then found for each galaxy. For E/S0 galaxies, this corresponding maximum likelihood redshift then provides a good estimate of the cluster redshift.

Once this list of cluster center likelihoods is assembled, these potential centers are ranked by decreasing maximum likelihood. The first cluster is seeded on the highest likelihood center, that cluster's BCG. Galaxies projected within a scaled radius, $R_{200}$, of this BCG and within $\pm 0.02$ in $z$ are eliminated from the list of potential centers. $R_{200}$ is the radius interior to which the mean density is 200 times the critical density ($\rho_{crit}$) as determined from SDSS galaxy populations (Hansen et al. 2005). The process is repeated for the next most likely BCG on the list, given that it has not been eliminated by a higher likelihood BCG, and continues likewise until all potential centers have either been labeled as cluster BCGs or have been subsumed by higher likelihood centers. Each cluster defined in this way has a center defined as the BCG location, an estimated redshift, and a richness, $N_{200}$, given by the number of E/S0 ridgeline members falling within $R_{200}$ of the BCG and brighter than $0.4\,L_*$. The final cluster catalog contains an array of measured properties, including photometric redshifts, richnesses, optical luminosities, and locations.

The public maxBCG catalog contains a total of 13,823 clusters drawn from approximately 7500 square degrees of sky between redshifts of 0.1 and 0.3, with a median redshift $\tilde{z} = 0.23$. The center for each cluster is defined as the location of the BCG identified by the algorithm. The richness of the cluster, $N_{200}$, ranges between 10 and 188 in the public catalog, and in principle extends down to $N_{200} = 1$ where the maxBCG selection function is less well-understood. For this study we include some clusters of lower richness, adding an additional 3532 clusters with $N_{200} = 9$. This slightly extended catalog allows us to use the same richness bins studied in the analysis of maxBCG galaxy dynamics (B07) and gravitational lensing (S07, J07).

Redshift estimates for the clusters, produced as part of the cluster finding process, have been shown by comparison to spectroscopic redshifts to be quite accurate, with $\Delta_z \leq 0.015$ (Koester et al. 2007a). Catalog completeness and purity have been studied in some detail in Rozo et al. (2007a); both are quite high. Completeness is estimated to be $\geq 90\%$ for clusters with masses greater than $10^{14}\,h^{-1}\,M_\odot$, and purity is $\geq 90\%$ for clusters with richnesses $N_{200} \geq 10$.

The cluster population in this catalog has been used to derive constraints on cosmology (Rozo et al. 2007a) using cluster counts. The relationship between the maxBCG richness $N_{200}$ and mass has been studied through galaxy dynamics (B07) and weak lensing (S07, J07). Further work on galaxy populations, mass-to-light ratios, and improved richness estimates for these clusters is in progress.

### 2.3. ROSAT *All-Sky Survey*

The *ROSAT* All-Sky Survey (RASS, Voges et al. 1999) was a six-month campaign in 1990-1991 to image the whole sky in soft X-rays (0.1-2.4 keV) with the ROSAT Position Sensitive Proportional Counter (PSPC, Pffeffermann et al. 1987). The survey scanned the sky in great circles, with the largest net exposure time ($\sim 40000\,\mathrm{s}$) near the ecliptic poles. The typical field coincident with the maxBCG survey region, which does not overlap the northern ecliptic pole, has an effective exposure time of $\sim 400\,\mathrm{s}$. The point spread function (PSF) for these RASS scans is very broad (full-width-half-maximum of $\sim 25''$) and is dominated by far off-axis photons due to the survey strategy. Voges et al. (2001) released reprocessed photon maps and exposure maps of the entire RASS survey region. These photon maps provide the input for the analysis described in this paper.

RASS data has been used to create several catalogs of purely X-ray selected objects. The ROSAT bright source catalog (BSC, Voges et al. 1999) consists of 18,811 sources with a typical signal-to-noise $> 4$. The position resolution is superior to the PSF FWHM with 68% (90%) of the sources within $13''$ ($25''$). In addition to the BSC, there is a companion Faint Source Catalog (FSC, Voges et al. 2000) consisting of 105,924 sources with a typical signal-to-noise $> 2$. Most are unresolved. Combined, these catalogs provide soft X-ray detected sources which can also be compared to the maxBCG clusters.

The RASS photon data has also been used as an input for X-ray flux-limited cluster catalogs. The Brightest Cluster Sample (BCS, Ebeling et al. 1998) is a flux-limited sample of the brightest 201 clusters in the northern hemisphere with fluxes $F_X > 5 \times 10^{-12}\,\mathrm{erg\,s^{-1}\,cm^{-2}}$. The Northern ROSAT All-Sky galaxy cluster survey (NORAS, Böhringer et al. 2000) is a catalog of 378 extended X-ray sources that have been confirmed to be clusters via optical follow-up. Due to the broad ROSAT PSF, this catalog is only $\sim 50\%$ complete at their stated flux limit, $F_X > 3 \times 10^{-12}\,\mathrm{erg\,s^{-1}\,cm^{-2}}$, which corresponds to a luminosity $L_X \gtrsim 1 \times 10^{44}\,h^{-2}\,\mathrm{erg\,s^{-1}}$ at our median redshift $\tilde{z} = 0.23$. Koester et al. (2007a) have performed an initial comparison between NORAS clusters and maxBCG clusters and have found that the maxBCG detects $> 90\%$ of NORAS objects. This is consistent with estimates of the completeness from simulations (Koester et al. 2007a; Rozo et al. 2007b). The *ROSAT*-ESO Flux Limited X-ray galaxy cluster survey (REFLEX: Böhringer et al. 2004) is similar to NORAS in the southern sky, with the same flux limit. This catalog of 447 clusters is over 90% complete due to improvements in RASS analysis, although only a small fraction of REFLEX overlaps the maxBCG survey area.

TABLE 1.  NUMBER OF CLUSTERS IN EACH BIN

| Richness Range[a] | $\bar{N}_{200}$ | $R_{200}$[b] $(h^{-1}\,\mathrm{kpc})$ | $N_{\mathrm{clust}}$ | $N_{\mathrm{stack}}$ |
|---|---|---|---|---|
| $71 \leq N_{200} \leq 188$ | 92.85 | 1727 | 55 | 55 |
| $51 \leq N_{200} \leq 70$ | 58.22 | 1469 | 146 | 140 |
| $41 \leq N_{200} \leq 50$ | 44.67 | 1317 | 207 | 201 |
| $33 \leq N_{200} \leq 40$ | 35.74 | 1201 | 356 | 339 |
| $26 \leq N_{200} \leq 32$ | 28.57 | 1102 | 665 | 633 |
| $21 \leq N_{200} \leq 25$ | 22.70 | 997 | 1128 | 1060 |
| $18 \leq N_{200} \leq 20$ | 18.91 | 941 | 1141 | 1099 |
| $12 \leq N_{200} \leq 17$ | 13.88 | 823 | 5651 | 5405 |
| $9 \leq N_{200} \leq 11$ | 9.80 | 727 | 7986 | 7566 |
| random | | | 7986 | 7529 |

[a] $N_{200}$ is the number of red-sequence galaxies brighter than 0.4 $L_*$ within a scaled aperture $R_{200}$.
[b] $R_{200}$ is the radius internal to which the mean density is 200 times the critical density (Hansen et al. 2005).

## 3. X-RAY ANALYSIS

The typical RASS exposure time for maxBCG clusters, 400 s, is too short to allow significant detections for individual clusters. The large number of maxBCG clusters, however, allows us to make up for this. For example, there are 7986 clusters with richnesses $9 \leq N_{200} \leq 11$. For these objects, the total RASS exposure time is $\approx 320,000$ s. Such a large total exposure allows us to measure the mean X-ray emission from these clusters quite precisely.

Details of the stacking method are described later in this section, and outlined here. We begin by dividing the clusters into nine richness ($N_{200}$) bins. To simplify comparison to other maxBCG analyses, we use the same richness bins used in measurements of the mean velocity dispersions (B07). The number of clusters in each richness bin is shown in Table 1.

As we do not have X-ray centers for individual clusters, we treat the BCG selected by the maxBCG algorithm as the center of each cluster and stack on these centers. In Koester et al. (2007a) it was shown that most maxBCG-selected BCGs ($\sim 80\%$) agree well with the center of X-ray selected clusters, which has also been seen for other optically-selected catalogs (e.g. Lin & Mohr 2004). Possible biases introduced by this assumption are discussed in Section 5.2. Every source and background photon in the stacked analysis is scaled and weighted to the median redshift of the clusters in the catalog, $\tilde{z} = 0.2296$. With these weighted photon maps we construct stacked images in Section 3.2, radial profiles in Section 3.3, and spectra and luminosities in Section 3.4.

### 3.1. *Cluster Extraction and Selection*

We obtain RASS photon data and merged exposure maps from the archives available at the High Energy Astrophysics Science Archive Research Center (HEASARC). The RASS data and exposure maps are distributed in $6.4 \times 6.4$ degree fields with significant overlap. Nevertheless, since we utilize a large background annulus extending to $40'$ from the central BCG, a significant fraction ($\sim 20\%$) of the maxBCG clusters fall across a field boundary. We have therefore built a tool that extracts all RASS photons in a given aperture, from multiple RASS fields if necessary, rejecting duplicate photons

in the overlap regions.[11] After photon retrieval, the appropriate merged exposure maps (mex file) are used to calculate the effective exposure time ($t_i$) at the position of each detected photon.

Before stacking we exclude from the list a subset of maxBCG clusters which might bias our X-ray measurements for unphysical reasons. No cut on Galactic absorption is required, as the SDSS observations are restricted to high galactic latitude. The typical equivalent Galactic hydrogen column density is a very low: $N_H = 2 \times 10^{20}\,\mathrm{cm}^{-2}$ (Dickey & Lockman 1990) for the maxBCG clusters, with a maximum of $N_H = 9 \times 10^{20}\,\mathrm{cm}^{-2}$. Although the typical RASS exposure time is $\sim 400$ s, there are some fields with significantly less. This makes source and background estimation difficult, while not adding significantly to the signal. For this reason, we reject all clusters with less than 200 s mean exposure time. This removes 4% of the total number of clusters, but less than 1% of the net exposure time.

An important possible source of contamination for stacked cluster measurements is the presence of a few extremely bright foreground sources. We would like to reject regions contaminated by these sources. RASS images of maxBCG clusters, especially at higher redshift, are often unresolved, making it difficult to remove point sources using extent information, so we proceed as follows. We first identify those ROSAT Bright Source Catalog (BSC) sources in the survey area with count rates higher than that expected for emission from any cluster at redshift beyond 0.1. This corresponds to a count rate of $\approx 2\,\mathrm{ct\,s^{-1}}$. There are 179 BSC sources in the maxBCG survey area with ROSAT soft-band (0.1-0.5 keV) or hard-band (0.5-2.1 keV) count rates above this limit. Of these 179 sources, only 13 are clusters as identified in the *ROSAT* Brightest Cluster Sample (BCS, Ebeling et al. 1998). Of these 13 clusters, only one of these objects is associated with a maxBCG cluster (Abell 2142, the richest and one of the nearest clusters in the catalog). The other bright clusters are at redshifts $z \ll 0.1$. Further visual inspection has confirmed that Abell 2142 is the only maxBCG cluster associated with one of these extremely bright sources. We reject as possibly contaminated all clusters (except for Abell 2142) within $45'$ of any of these bright sources. This removes only 0.6% of the maxBCG catalog.

The Virgo cluster is another important foreground source. This nearby, X-ray bright cluster dominates the RASS emission over a significant region of sky, thus making it difficult to estimate the X-ray emission from background clusters. We therefore reject all clusters that fall within 1.5 degrees of M86 or M87. This is a relatively small effect, removing only 0.1% of the maxBCG clusters. Table 1 shows the number of clusters in each richness bin before and after the rejections outlined in this section, as well as the mean richness for each bin.

To stack the X-ray measurements of the clusters, RASS photons from each cluster must be scaled and appropriately weighted. The projected physical distance to the BCG is calculated for each photon, and this scaled distance is used in image construction and radial profile cal-

[11] RASS photons are tagged with the detector location, energy channel, and time of arrival, providing a unique description of each photon.

culations. Each source and background photon is then weighted by a factor of $w(z) = (d_L(z)/d_L(\tilde{z}))^2$, where $d_L(z)$ is the luminosity distance to the cluster and $d_L(\tilde{z})$ is the luminosity distance to the median cluster redshift $\tilde{z} = 0.2296$. For background estimation we use a fixed annulus with inner (outer) radius of $20'$ ($40'$), similar to that used for the NORAS catalog for individual clusters (Böhringer et al. 2000). This background annulus corresponds to a physical distance of $1.5 - 3.1 \, h^{-1}$ Mpc at our minimum redshift of 0.1 and a $3.8 - 7.5 \, h^{-1}$ Mpc at our maximum redshift of 0.3. We confirm that our results are not sensitive to the exact choice of background annulus. To calculate the weighted count rate ($C_w$) in a given bin (image, radial, or spectral) for a cluster at redshift $z$, we follow a procedure similar to Böhringer et al. (2000), where $C_w = \sum_i w(z_i)/t_i$, where $t_i$ is the exposure time at the position of each detected photon.

As a simple test of our stacking procedure, we also extract RASS photons from a set of positions selected at random from the region covered by the maxBCG catalog. Each such random position is associated with a real cluster redshift drawn from the catalog in the $9 \leq N_{200} \leq 11$ bin. The random points are analyzed identically to the real cluster positions.

### 3.2. Stacked X-Ray Images

The background-subtracted stacked images are shown in Figure 1. Each image has a projected radius of $2.0 \, h^{-1}$ Mpc. The images contain photons from the *ROSAT* hard band (channels 51-201, 0.5-2.0 keV) as this band has the highest signal-to-noise for cluster emission. After background subtraction, the counts were put in $100 \times 100 \, h^{-1}$ kpc bins. For display, each image has been scaled with histogram equalization to show similar background noise levels, as there are two orders of magnitude more clusters in the poorest bin than the richest bin. The contours are drawn $3\sigma$ and $5\sigma$ above background level.

Highly significant X-ray emission is seen in each stack of clusters. By contrast, in a stack of 7,566 random points there is no significant excess, and no sign of emission centered in the stack. It is worth noting that the average count rate in the $9 \leq N_{200} \leq 11$ bin is only $0.0025 \, \mathrm{ct \, s^{-1}}$, corresponding to a flux $F_X = 5 \times 10^{-14} \, \mathrm{erg \, s^{-1} cm^{-2}}$. There are a total of $\sim 8500$ cts in excess of background from $\sim 8000$ clusters; an average of only 1 source count per cluster. This illustrates the power of the stacking exercise to probe very low count rates, and allows us to use RASS to measure very low $L_X$ cluster emission even at a moderate redshift of $\sim 0.2$.

### 3.3. Radial Profiles

Figure 2 presents the background-subtracted surface-brightness profiles for the stacked X-ray images in each richness bin, summed in $50 \, h^{-1}$ kpc bins. Significant cluster X-ray emission is seen in each richness bin, out to distances of $\sim 1.5 \, h^{-1}$ Mpc. The X-ray surface brightness profiles for the different bins look remarkably similar, except for the normalization which increases strongly with richness and the signal-to-noise which decreases slowly with richness. We fit the surface brightness profiles out to $1.5 \, h^{-1}$ Mpc with a standard $\beta$ model, $S(R) = S_0(1 + R^2/R_C^2)^{-3\beta + 1/2}$. The best-fit parameters are presented in Table 2, and are overplotted with dashed

TABLE 2. $\beta$ MODEL PARAMETERS

| Richness Range | $\beta$ | $R_c (h^{-1} \text{ Mpc})$ | $\chi^2/\nu$ |
|---|---|---|---|
| $71 \leq N_{200} \leq 188$ | $0.67 \pm 0.03$ | $0.31 \pm 0.03$ | 37.7/72 |
| $51 \leq N_{200} \leq 70$ | $0.55 \pm 0.03$ | $0.23 \pm 0.02$ | 43.2/72 |
| $41 \leq N_{200} \leq 50$ | $0.62 \pm 0.04$ | $0.28 \pm 0.03$ | 36.2/72 |
| $33 \leq N_{200} \leq 40$ | $0.64 \pm 0.04$ | $0.31 \pm 0.03$ | 75.1/72 |
| $26 \leq N_{200} \leq 32$ | $0.57 \pm 0.03$ | $0.24 \pm 0.03$ | 46.3/72 |
| $21 \leq N_{200} \leq 25$ | $0.75 \pm 0.08$ | $0.40 \pm 0.05$ | 88.1/72 |
| $18 \leq N_{200} \leq 20$ | $0.51 \pm 0.03$ | $0.21 \pm 0.03$ | 38.9/72 |
| $12 \leq N_{200} \leq 17$ | $0.57 \pm 0.03$ | $0.24 \pm 0.03$ | 36.2/72 |
| $9 \leq N_{200} \leq 11$ | $0.54 \pm 0.04$ | $0.22 \pm 0.04$ | 63.4/72 |

lines in Figure 2. The $\beta$ model results in a good fit in all cases.

The core radii, $R_c$, for these $\beta$ model fits are surprisingly large, ranging from $\sim 200 \, h^{-1}$ kpc to $\sim 400 \, h^{-1}$ kpc. These are significantly larger than those typically seen for X-ray clusters ($\sim 50 - 150 \, h^{-1}$ kpc, e.g. Neumann & Arnaud 1999). While the $\beta$ parameters are typical for X-ray clusters (e.g. Neumann & Arnaud 1999; Sanderson et al. 2003), there is no significant change in $\beta$ with richness. Previous work has hinted at a dependence of $\beta$ on mass (Horner et al. 1999; Helsdon & Ponman 2000; Sanderson et al. 2003), although DKM07 measure core radii and $\beta$ values that are very similar to what we measure. These somewhat surprising results are caused by two effects; the broad point spread function for RASS objects, and the offset distribution between the BCG and the X-ray cluster emission.

#### 3.3.1. RASS PSF effects

To study the effect of the RASS PSF on the stacked profiles, we test our analysis on bright ROSAT point sources. These sources were selected from the WGA catalog (White et al. 2000), which contains 88,621 well measured point-like sources selected from ROSAT PSPC pointed observations. We take $\sim 500$ moderately bright $(0.1 - 0.5 \, \mathrm{ct \, s^{-1}})$ point sources that overlap the SDSS DR5 mask. These bright sources are also well detected in RASS. Each point source is randomly assigned a redshift drawn from the maxBCG cluster catalog redshift distribution. The point sources are then stacked in exactly the manner described for clusters above. Figure 3 shows the radial profile of the stacked point sources (diamonds). While this radial profile is much more sharply peaked than that of the stacked clusters, the broad ROSAT PSF scatters significant X-ray emission to distances $> 1 \, h^{-1}$ Mpc ($7'$ at $z = 0.2$) from the center. This PSF smearing implies an effective minimum on the $\beta$-model core radius, as well as creating a possible bias in the calculation of the $\beta$ parameter. We note that $\lesssim 10\%$ of the selected WGA point sources are within $10'$ of maxBCG clusters. Excluding the point sources that are neighboring these possibly extended X-ray sources does not significantly alter this result.

#### 3.3.2. Optical / X-ray offsets

The stacked, projected surface brightness profile may also be affected by our choice of cluster centers. There are several ways in which the BCG chosen by the maxBCG algorithm might be offset from the X-ray emission from
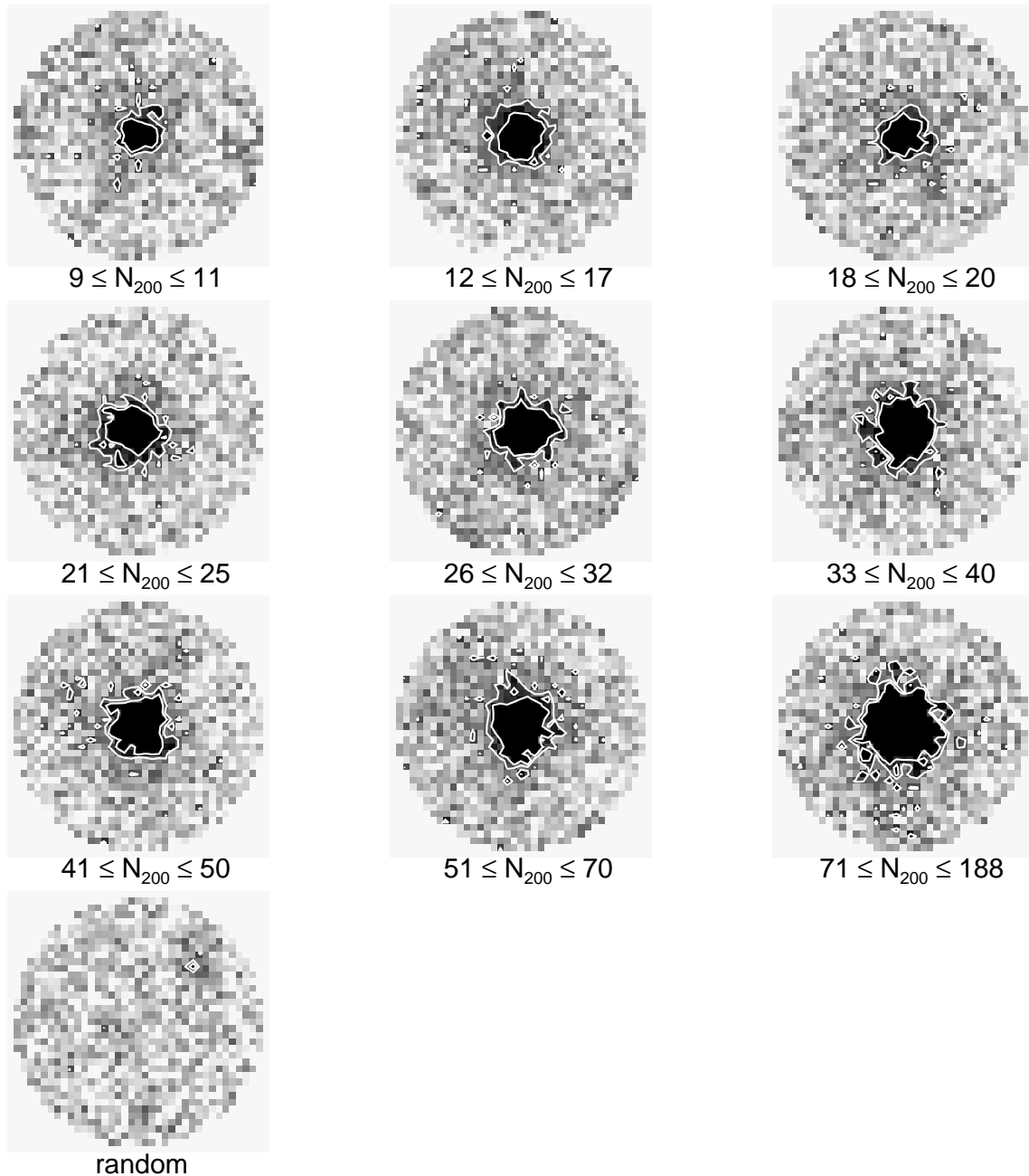
<table>
9 ≤ N_{200} ≤ 11
</table>

FIG. 1.— Stacked X-ray images for the 9 richness bins and random points. Each image has a projected radius of $2.0\,h^{-1}\,\mathrm{Mpc}$. The *ROSAT* hard band (0.5-2.0 keV) counts have been background subtracted and put in $100 \times 100\,h^{-1}\,\mathrm{kpc}$ bins. For display, each image has been scaled with histogram equalization to show similar background noise levels. The contours are drawn $3\sigma$ and $5\sigma$ above background level.

the cluster. Dynamically active clusters and clusters in the process of merging can have a significant offset between the X-ray centroid and the BCG. There is also the possibility that the maxBCG algorithm chose an incorrect center (this is addressed more fully in Section 5.2). In addition, there may be additional X-ray point sources such as AGN that are associated with the clusters. All of these effects result in an effective optical/X-ray offset distribution that may bias the radial profiles.

We model the optical/X-ray offset distribution by matching the maxBCG catalog to known X-ray sources. For this exercise, we use the fact that many maxBCG clusters ($> 900$) are associated with individual detections in the ROSAT Bright Source and Faint Source Catalogs. Most of these BSC and FSC sources have not been previously recognized as associated with clusters, primarily because they are too faint or too distant to be seen as significantly extended in RASS. We match the maxBCG clusters to the BSC and FSC catalogs, allowing multiple X-ray sources to match to each cluster. This ensures that
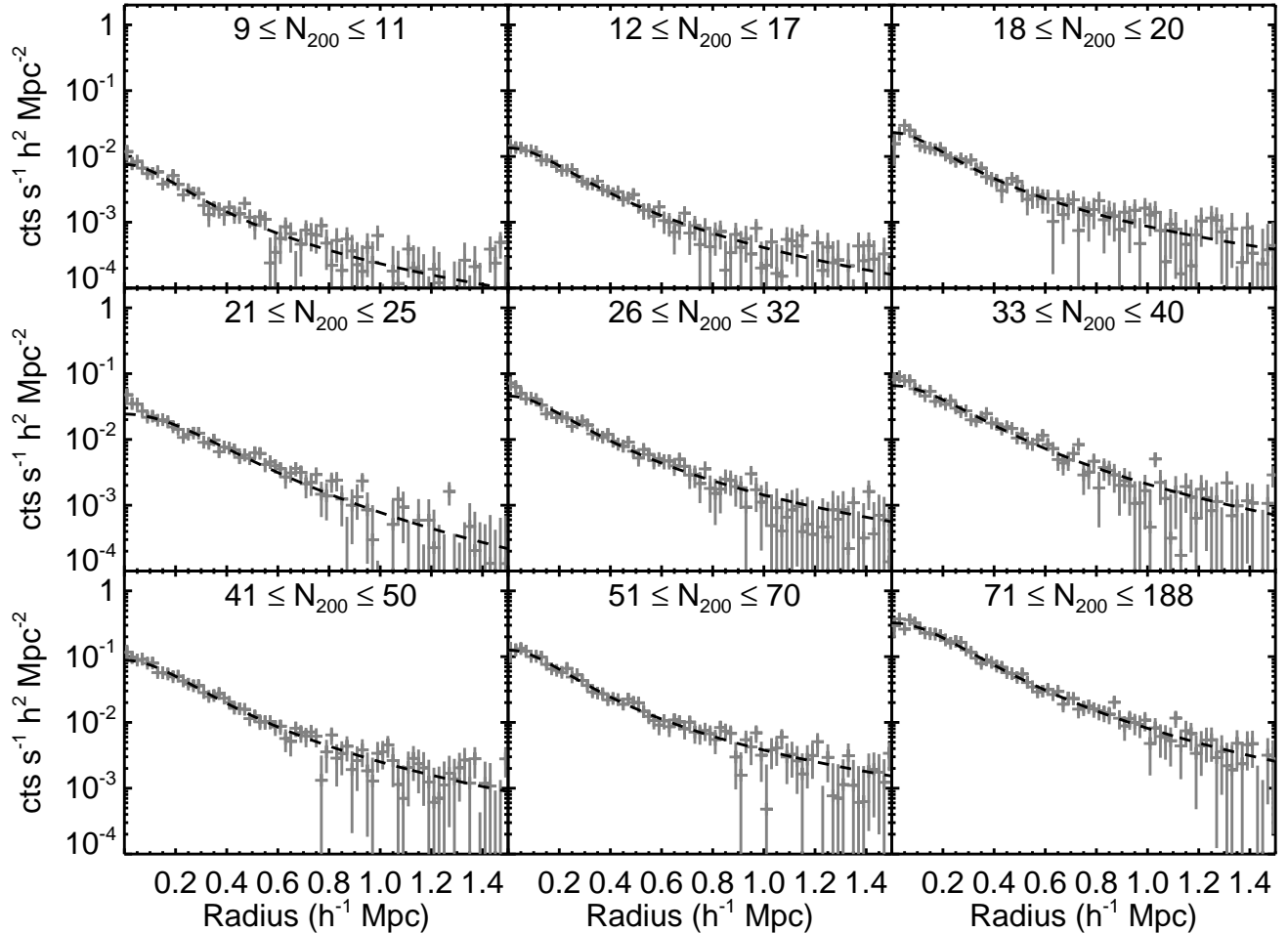
FIG. 2.— The background subtracted surface brightness profiles for the stacked images, in $50\,h^{-1}$ kpc bins. Significant cluster emission is seen in each richness bin, out to distances of $\sim 1.5\,h^{-1}$ Mpc. The dashed lines show the $\beta$ model fits from Table 2.

we find all X-ray sources associated with each cluster, as well as all possible random matches. We similarly match an equal number of random locations drawn from the maxBCG survey region to the BSC and FSC catalogs. Figure 4 shows the projected offset distribution from the maxBCG clusters to the BSC and FSC catalogs. The solid (dashed) line shows a histogram of maxBCG (random) offsets in $50\,h^{-1}$ kpc bins. The dotted line shows the residual distribution after subtracting the random matches from the cluster matches.

The subtracted histogram in Figure 4 shows a large excess of X-ray sources associated with the optical cluster centers. There is a tight core in which the BCG is within $\sim 150\,h^{-1}$ kpc of an X-ray source, as well as a long tail extending out to $\sim 1500\,h^{-1}$ kpc. The X-ray source excess at large radius is likely to be associated with the maxBCG clusters. These sources comprise a mix of merging clusters, clusters with poorly identified centers, and associated point sources such as AGN. The subtracted histogram is used as a first-order empirical radial distribution of X-ray sources associated with maxBCG cluster centers.

We now estimate the additional effect on the radial pro-

file due to the radial offset distribution of X-ray sources associated with the maxBCG clusters. We take each WGA point source from Section 3.3.1 and randomly alter its position so that the distribution is offsets is identical to the empirical radial distribution. These offset point sources are run through our stacking analysis. Figure 3 shows the radial profile of the offset point sources after stacking (circles). This radial profile is reasonably well fit with a $\beta$ model, although the fit is poor within $\sim 200\,h^{-1}$ kpc. At large radii the radial profile is well fit with $\beta = 0.61 \pm 0.01$. Thus, at large radii it is not possible to distinguish between true *extended* cluster emission and X-ray *point* sources convolved with the observed maxBCG–X-ray source offset distribution.

This calls into question the utility of the $\beta$ model parameterization for this exercise. The stacked X-ray profile is a convolution of the ROSAT PSF, the centering distribution, and the true extended X-ray emission. Operationally, it is not possible to separate the contributions from these three components. Therefore, the $\beta$ parameters that are the result of a stacking exercise such as this one, where most of the individual X-ray clusters are not detected, should be used cautiously.
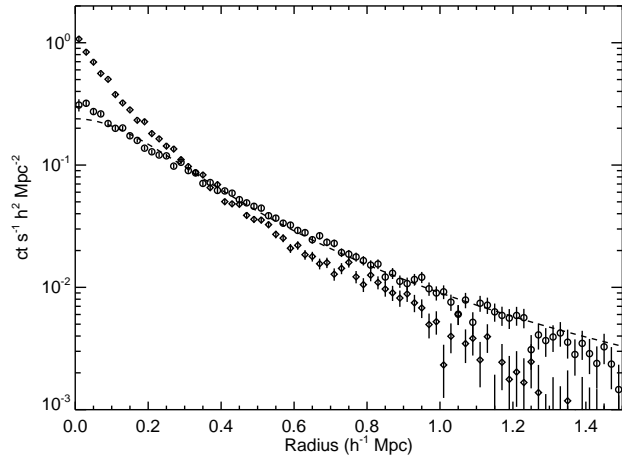
Rykoff et al.



FIG. 3.— The radial profile of stacked point sources selected from the WGA (White et al. 2000) catalog. Each point source has been randomly assigned a redshift from the maxBCG redshift distribution to simulate the effect of smearing due to radial scaling. The diamonds show the stacked point source profile with the centers as determined in WGA; there is significant emission out to distances $> 1\,h^{-1}\,\mathrm{Mpc}$ ($7'$ at $\tilde{z} = 0.22$). The circles show the stacked point source profile after convolving with the estimated maxBCG/BSC-FSC offset distribution. The outer profile is well-fit by a $\beta$-model (dashed line) with $\beta = 0.61 \pm 0.01$. Thus, a cluster-like radial profile is obtainable in stacked images even without true extended cluster emission.
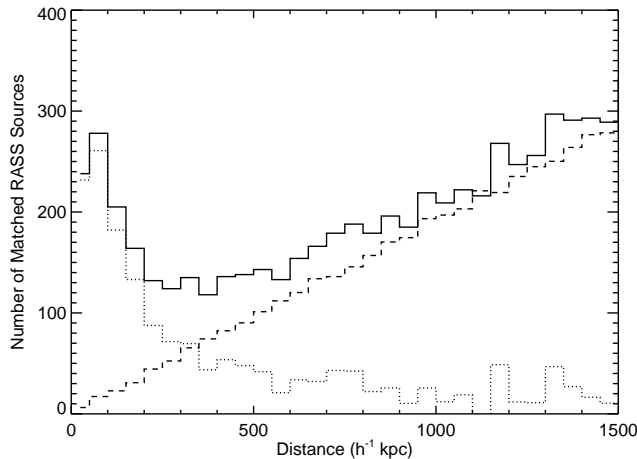


FIG. 4.— Histogram of offset distribution between maxBCG clusters and X-ray sources detected in the BSC and FSC catalogs. Each cluster is allowed to match to multiple X-ray sources, ensuring we find all associated X-ray sources in addition to all random matches. The solid (dashed) line shows the histogram of maxBCG (random) offsets in $50\,h^{-1}$ kpc bins. The dotted line shows the result of subtracting the random matches from the cluster matches. There is a tight core in which the BCG is within $\sim 150\,h^{-1}$ kpc of an X-ray source, as well as a long tail.

### 3.4. *Stacked X-ray Spectra*

We perform spectral fitting of the photons in each stack to calculate X-ray luminosities. The spectra were analyzed using XSPEC version 11.3.2 (Arnaud 1996). Spectral analysis on the stacked ROSAT data involves a variety of complications, some of which are discussed in DKM07. We outline some key issues here.

All RASS observations integrate exposure time across the *ROSAT* field-of-view. As a result, we use the spectral response file `pspcc_gain1_256.rmf` from HEASARC, suitable for off-axis observations. When combined with the appropriate ancillary response file (`arf`), we obtain the vignetting corrected spectral response for the off-axis photons that comprise our spectra. However, the exposure times extracted from the merged exposure maps for RASS are already corrected for vignetting, using the mean spectrum of the X-ray background in the PSPC band[12]. In practice, this means that our spectra, fit with the standard `rmf`+`arf` combination, are corrected for vignetting *twice* – once by using the exposure times obtained from the merged exposure map, and once in the calculation of the `arf` file. By comparing the on-axis response file `rsp` from HEASARC with the combination of the `rmf`+`arf` we can approximate the extra vignetting correction. This correction is a function of energy, and depends (weakly) on the spectrum of the observed source. By simulating cluster spectra of various temperatures, we calculate the typical correction factor averaged across the ROSAT hard band (0.5-2.0 keV) which is dominated by cluster flux. This correction factor is $\sim 1.53$. Using this correction factor results in very good agreement between our spectral analysis and the REFLEX count-rate to flux conversion tables of Böhringer et al. (2004). We estimate that applying this correction factor to all flux and luminosity values determined from stacked spectra adds an additional systematic error of $\sim 10\%$.

For our analysis, we use the `rmf` file described above, combined with an `arf` output with the FTOOL `pcarf`. As noted in DKM07, each `arf` file is essentially identical, because each stacked cluster from RASS samples photons from the entire ROSAT field of view. Spectral files are then grouped with a minimum of 50 counts per bin (after background subtraction) to ensure valid results using $\chi^2$ statistical analysis. Fits performed with XSPEC were restricted to the 0.1-2.1 keV range. The uncertainties in spectral fit parameters are 90% confidence errors, obtained by allowing all fit parameters to vary simultaneously.

We obtain cluster spectra by summing all weighted cluster photons in both fixed physical apertures and scaled apertures of the optically determined $R_{200}$ (see Section 2.2). The fixed aperture of $750\,h^{-1}$ kpc is chosen as a reasonable fiducial value because this provides good signal-to-noise, and because the radial profiles do not appear to change significantly with richness. The $R_{200}$ value for each bin was taken as the median $R_{200}$ of all the clusters in the richness bin; these values are reported in Table 3. Background spectra are stacked with the same weights as the source spectra, using the annuli defined in Section 3.1. As described previously, each photon is weighted to the median redshift $\tilde{z} = 0.2296$. Unfortunately, k-correction of individual photons is not possible, due to the fact that the detection channel of the incident photons is most strongly dominated by the spectral response of the ROSAT instrument. The stacking procedure will therefore tend to "smear out" the incident cluster spectra. Simple simulations of X-ray spectra using XSPEC show that this does not create a large effect

---

[12] see the manual page for the FTOOL `pcexpmap`

on our best-fit spectral values, as our redshift range of $0.1 < z < 0.3$ is not particularly broad. Similarly, we do not make any corrections for possible redshift evolution in X-ray luminosity; we will address this further in Section 5.3.

The spectra are fit with an absorbed thermal plasma model (Raymond & Smith 1977). The metallicity is fixed at 0.3 solar (e.g. Anders & Grevesse 1989), and the redshift is set to the median scaled redshift of 0.2296. The luminosities are calculated in the rest-frame 0.1-2.4 keV band at the median redshift. We prefer to calculate the 0.1-2.4 keV luminosity rather than bolometric luminosity ($L_{X,\text{bolo}}$), due to the large extrapolations required to obtain bolometric values, which strongly depend on spectral temperatures (see below). The best-fit spectral parameters for the scaled $R_{200}$ apertures are shown in Table 3, and the parameters for the fixed $750\,h^{-1}$ kpc apertures are shown in Table 4.

In order to account properly for the variations in cluster luminosity in each richness bin, we use bootstrap resampling to estimate the luminosity errors. In each richness bin, we run 2000 trials by sampling the same number of clusters in that bin with replacement. To save considerable time with processing, we did not recreate the entire stacking procedure for each resampling. Instead, we take the individual cluster counts, scaled to the median redshift. We confirm that the average scaled count rate is a good proxy for luminosity in the 0.1-2.4 keV band (see Section 4.1 for details on this calculation). The 68% ($1\sigma$) confidence interval obtained from the bootstrap is added in quadrature with the $L_X$ errors obtained from the spectral fits. Only the richest ($71 \leq N_{200} \leq 188$) bin is dominated by the bootstrap error calculation, due to the large range in richness and $L_X$ in the bin.

Figure 5 shows the mean $\bar{L}_X$–$\bar{T}_X$ relation for our stacked clusters (within the scaled $R_{200}$ aperture), compared to the Markevitch (1998) $L_X$-$T_X$ (0.1-2.4 keV) relation. We see the cluster temperature increase with luminosity, but our observed $\bar{L}_X$–$\bar{T}_X$ relation is noticeably steeper than that of Markevitch (1998). The stacked X-ray temperatures appear to underestimate the expected temperature, especially at $\bar{L}_X$ larger than a few times $10^{43}\,h^{-2}\,\text{ergs s}^{-1}$. This discrepancy highlights the challenge of measuring cluster temperatures with ROSAT, as well as the challenges of measuring stacked cluster temperatures. First, ROSAT has sensitivity only to soft X-rays. When the break of the bremsstrahlung spectrum, determined by the temperature of the hot gas, is above $\sim 2.0\,\text{keV}$, then the X-ray temperature becomes difficult to constrain. The *ROSAT* temperatures of hot clusters are generally underestimated; a particular example is Abell 1689. This bright cluster has a nearly isothermal profile in *XMM/Newton* observations with a temperature of $\sim 9\,\text{keV}$ (consistent with the ASCA and *Chandra* values), but has a best-fit *ROSAT*/PSPC temperature of $4.3^{+1.2}_{-0.8}\,\text{keV}$ (e.g. Andersson & Madejski 2004). Second, when we stack many non-isothermal clusters with different temperatures, our isothermal Raymond-Smith spectrum is no longer appropriate. For example, Rasia et al. (2005) have shown for *Chandra* observations how the spectroscopically-weighted temperature can differ significantly from the emission-weighted temperature for single clusters, with the better measured colder gas dominating
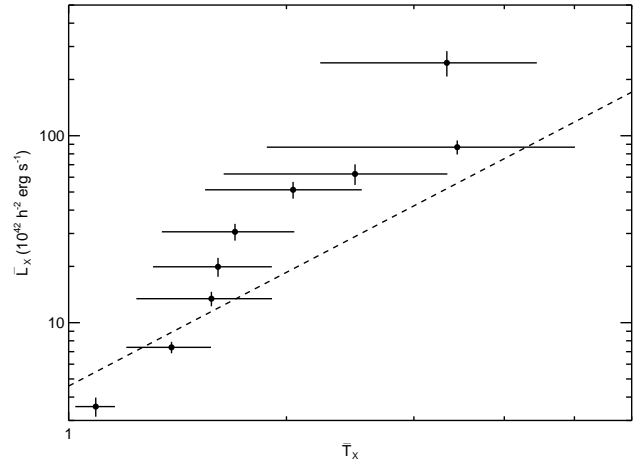


FIG. 5.— Mean $\bar{L}_X$–$\bar{T}_X$ relation for the stacked clusters, with the fits within $R_{200}$. The dashed line shows the Markevitch (1998) relationship for "uncorrected" 0.1-2.4 keV luminosity. The observed relation is much steeper than that derived by Markevitch (1998). This is due to the fact that *ROSAT* temperatures tend to underestimate cluster temperatures with $T_X \gtrsim 3\,\text{keV}$, as well as the complications in stacking many clusters with different temperatures.

the spectral fit. When these effects are combined, interpreting the average best-fit spectral temperature from a stack of hundreds of clusters is non-trivial. All this suggests that calculating 0.1-2.4 keV $L_X$ obtained from *ROSAT*—which relies primarily on photon counting—is more robust than calculating $T_X$ and extrapolating to $L_{X,\text{bolo}}$. Although a small $k$-correction ($\sim 10\%$) is required to extrapolate from observer frame 0.1-2.4 keV to rest-frame luminosity, this correction is not very sensitive to the spectral temperature at the moderate redshift of the maxBCG clusters.

## 4. MEAN $\bar{L}_X$–$\bar{N}_{200}$ RELATION

We stack the clusters and calculate the 0.1-2.4 keV X-ray luminosity as described in the previous section. Figure 6 shows the mean $\bar{L}_X$–$\bar{N}_{200}$ relation, both for a fixed $750\,h^{-1}$ kpc aperture and for the scaled $R_{200}$ apertures. We find a strong correlation between $\bar{L}_X$ and $\bar{N}_{200}$ with both the fixed and the scaled apertures. In the low richness bins ($N_{200} \leq 17$), the scaled aperture $R_{200}$ is approximately equal to the fixed $750\,h^{-1}$ kpc aperture, and $\bar{L}_X$ is approximately the same for both choices of aperture. In the high richness bins, the scaled aperture $R_{200}$ is significantly larger than $750\,h^{-1}$ kpc, yielding a slightly larger $\bar{L}_X$ for the scaled apertures. For this reason, the $\bar{L}_X$–$\bar{N}_{200}$ relation is slightly steeper using scaled apertures. The best-fit mean relationships are:

$$\bar{L}_X(< R_{200}) = e^{3.87 \pm 0.04} \left( \frac{N_{200}}{40} \right)^{1.82 \pm 0.05} 10^{42}\,h^{-2}\,\text{ergs s}^{-1}$$

$$(1)$$

$$\bar{L}_X(< 750\,h^{-1}\,\text{kpc}) = e^{3.63 \pm 0.04} \left( \frac{N_{200}}{40} \right)^{1.64 \pm 0.05} 10^{42}\,h^{-2}\,\text{ergs s}^{-1}$$

$$(2)$$

Power law fits are chosen to pivot around $N_{200} = 40$ to approximately decouple errors in slope and normalization.

Rykoff et al.

TABLE 3. SPECTRAL FITS WITHIN $R_{200}$

| Richness Range | $\bar{N}_{200}$ | $R_{200}$ ($h^{-1}$ Mpc) | $N_H$ ($10^{20}$ cm$^{-2}$) | kT (keV) | $\bar{L}_X$ ($10^{42}$ $h^{-2}$ ergs s$^{-1}$) | $\chi^2/\nu$ |
|---|---|---|---|---|---|---|
| $71 \leq N_{200} \leq 188$ | 92.85 | 1.73 | $2.5 \pm 0.4$ | $3.3^{+1.4}_{-0.9}$ | $228 \pm 33$ | 47.2/76 |
| $51 \leq N_{200} \leq 70$ | 58.22 | 1.47 | $1.5 \pm 0.3$ | $3.4^{+2.1}_{-1.1}$ | $80.6 \pm 6.9$ | 61.5/77 |
| $41 \leq N_{200} \leq 50$ | 44.67 | 1.32 | $2.8^{+0.7}_{-0.6}$ | $2.5^{+1.1}_{-0.6}$ | $58.0 \pm 7.3$ | 87.4/65 |
| $33 \leq N_{200} \leq 40$ | 35.74 | 1.20 | $2.8^{+0.6}_{-0.4}$ | $2.0^{+0.6}_{-0.4}$ | $47.7 \pm 4.8$ | 100.6/95 |
| $26 \leq N_{200} \leq 32$ | 29.57 | 1.10 | $3.4^{+0.9}_{-0.6}$ | $1.7^{+0.4}_{-0.3}$ | $28.4 \pm 3.0$ | 62.9/95 |
| $21 \leq N_{200} \leq 25$ | 22.70 | 0.99 | $3.2^{+0.9}_{-0.6}$ | $1.6^{+0.4}_{-0.2}$ | $18.5 \pm 2.1$ | 113.2/97 |
| $18 \leq N_{200} \leq 20$ | 18.91 | 0.94 | $1.5^{+0.4}_{-0.3}$ | $1.6^{+0.4}_{-0.2}$ | $12.5 \pm 1.1$ | 77.3/88 |
| $12 \leq N_{200} \leq 17$ | 13.88 | 0.82 | $2.0^{+0.4}_{-0.3}$ | $1.4^{+0.3}_{-0.1}$ | $6.84 \pm 0.47$ | 182.3/134 |
| $9 \leq N_{200} \leq 11$ | 9.80 | 0.73 | $2.0^{+0.7}_{-0.5}$ | $1.1^{+0.08}_{-0.06}$ | $3.30 \pm 0.39$ | 127.8/112 |

TABLE 4. SPECTRAL FITS WITHIN $750\,h^{-1}$ kpc

| Richness Range | $\bar{N}_{200}$ | $R_{200}$ ($h^{-1}$ Mpc) | $N_H$ ($10^{20}$ cm$^{-2}$) | kT (keV) | $L_X$ ($10^{42}$ $h^{-2}$ ergs s$^{-1}$) | $\chi^2/\nu$ |
|---|---|---|---|---|---|---|
| $71 \leq N_{200} \leq 188$ | 92.85 | 1.73 | $1.8 \pm 0.3$ | $3.1^{+1.1}_{-0.7}$ | $167 \pm 24$ | 40.5/61 |
| $51 \leq N_{200} \leq 70$ | 58.22 | 1.47 | $1.6 \pm 0.3$ | $3.8^{+2.2}_{-1.1}$ | $57.3 \pm 4.9$ | 40.1/59 |
| $41 \leq N_{200} \leq 50$ | 44.67 | 1.32 | $2.2 \pm 0.4$ | $2.6^{+1.1}_{-0.6}$ | $45.6 \pm 5.6$ | 85.6/61 |
| $33 \leq N_{200} \leq 40$ | 35.74 | 1.20 | $2.3 \pm 0.4$ | $2.5^{+0.8}_{-0.5}$ | $38.8 \pm 3.9$ | 92.0/81 |
| $26 \leq N_{200} \leq 32$ | 28.57 | 1.10 | $3.0 \pm 0.6$ | $1.8^{+0.5}_{-0.2}$ | $23.4 \pm 2.3$ | 78.1/84 |
| $21 \leq N_{200} \leq 25$ | 22.70 | 0.99 | $2.6 \pm 0.5$ | $1.7^{+0.4}_{-0.2}$ | $16.4 \pm 1.8$ | 86.0/94 |
| $18 \leq N_{200} \leq 20$ | 18.91 | 0.94 | $2.0 \pm 0.5$ | $1.5^{+0.4}_{-0.2}$ | $10.9/pm0.9$ | 73.6/76 |
| $12 \leq N_{200} \leq 17$ | 13.88 | 0.82 | $2.0 \pm 0.3$ | $1.4^{+0.3}_{-0.1}$ | $6.50 \pm 0.45$ | 182.3/134 |
| $9 \leq N_{200} \leq 11$ | 9.80 | 0.73 | $2.1 \pm 0.7$ | $1.1^{+0.2}_{-0.06}$ | $3.40 \pm 0.42$ | 137.6/114 |
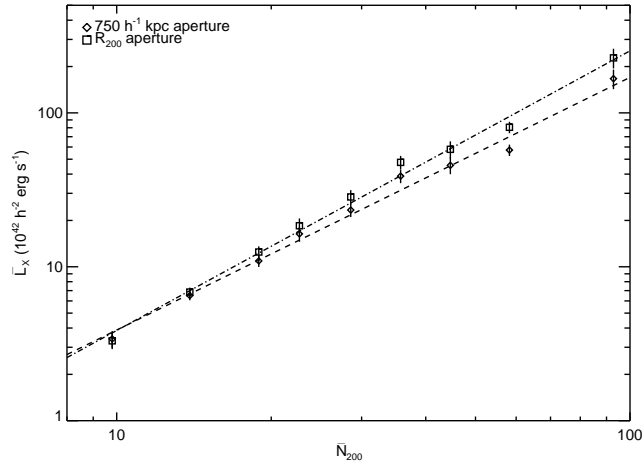


FIG. 6.— Mean $\bar{L}_X$–$\bar{N}_{200}$ relation for maxBCG clusters, for the fixed $750\,h^{-1}$ kpc apertures (diamonds) and the scaled $R_{200}$ apertures (squares). There is a strong correlation between $\bar{L}_X$ and $\bar{N}_{200}$, with a slope of $1.64\pm0.05$ ($750\,h^{-1}$ kpc) or $1.82\pm0.05$ ($R_{200}$). The scaled aperture relation is steeper because the aperture scales with $N_{200}$.

ity and richness definitions we employ, but a first-order conversion is possible. First, we convert the DKM07 bolometric luminosities (their Table 2) to *ROSAT* 0.1-2.4 keV luminosities using Table 5 of Böhringer et al. (2004)[13] Re-fitting for the $\bar{L}_X$–$\bar{N}_{*666}$ relation, we find $\bar{L}_X \propto (\bar{N}_{*666})^{1.51\pm0.07}$.[14] As the 2MASS catalog is not yet public, we cannot make a direct comparison of $N_{200}$ to $N_{*666}$ for individual clusters. Futhermore, most of the clusters in the 2MASS catalog are at $z < 0.1$, while the maxBCG catalog covers $0.1 \leq z \leq 0.3$. At this time, the most we can say is that the slope of the $\bar{L}_X$–richness relation is roughly similar between our work and DKM07.

### 4.1. Scatter in the $L_X$–$N_{200}$ Relation

Comparisons to X-ray selected catalogs (see Section 4.2) as well as prior studies (e.g. Smail et al. 1998; Gilbank et al. 2004) lead us to expect significant scatter in the X-ray luminosity–richness relation for individual clusters. With a large scatter, the mean statistic used to calculate the stacked $\bar{L}_X$–$\bar{N}_{200}$ relation is biased relative to the median relation. To understand this bias, we first assume that there is a log-normal conditional probability

[13] This does not introduce any additional error, as DKM07 have published the precise spectral temperature they used to calculate $L_{X,\text{bolo}}$.

[14] We note that the soft band $\bar{L}_X$–$\bar{N}_{*666}$ relation does not deviate from a power-law at any richness, unlike the $\bar{L}_{X,\text{bolo}}$–$\bar{N}_{*666}$ relation in Figure 10 of DKM07.

DKM07 also found that the mean X-ray luminosity of the 2MASS clusters scales with optical richness ($N_{*666}$). A direct comparison between the DKM07 relation and our relation is challenging, due to the different luminos-

$p$ for the X-ray luminosity of a cluster at richness $N_{200}$:

$$p(L_x|N_{200}) = \frac{1}{\sqrt{2\pi}\sigma_{\ln L}} \exp\left[\frac{-(\ln L_X - \overline{\ln L_X})^2}{2\sigma_{\ln L}^2}\right], \quad (3)$$

with constant intrinsic scatter $\sigma_{\ln L}$, and mean log luminosity that follows:

$$\overline{\ln L_X}(N_{200}) = A + B\ln(N_{200}/40), \quad (4)$$

where $A$ is the log normalization of $L_X$ at $N_{200} = 40$, and $B$ is the slope of the $L_X$–$N_{200}$ relation. Note that $\exp(\overline{\ln L_X})$ for a log-normal distribution is equivalent to the median (and geometric mean) of the distribution. For the duration of this paper, we employ the notation $\widetilde{L}_X \equiv \exp(\overline{\ln L_X})$.

At a given richness, the median X-ray luminosity ($\widetilde{L}_X$) is the quantity we desire, as this is the peak in the underlying log-normal distribution. However, the stacking exercise we have undertaken is fundamentally a calculation of the *arithmetic mean* ($\bar{L}_X$) at a given $\bar{N}_{200}$. For a log-normal distribution with median $\widetilde{L}_X$ and intrinsic scatter $\sigma_{\ln L}$, the arithmetic mean is $\exp(\overline{\ln L_X} + \sigma_{\ln L}^2/2)$. Thus, the stacked normalization overestimates the median of the true underlying distribution by a factor of $\exp(\sigma_{\ln L}^2/2)$. If the scatter is large, the stacked (mean) normalization will be biased high. For example, an 80% scatter indicates a $\sim 30\%$ bias.

To constrain this scatter, we begin with measurements of X-ray flux (and hence $L_X$) at the locations of each cluster with $N_{200} \geq 30$. Though many of these are low signal-to-noise detections, they can be used to measure scatter. The IDL Astronomy library tool `linmix_err` is used to fit $L_X$ as a function of $N_{200}$ with intrinsic scatter $\sigma_{\ln L}$ (Kelly 2007). This tool uses a Bayesian approach to linear regression with errors in X and Y and is well behaved even when the measurement errors dominate. It also handles non-detections and upper limits in Y. Monte Carlo simulations show that the selected $N_{200}$ cut provides a large enough richness range to constrain the slope and scatter, and provides larger signal-to-noise than the entire cluster catalog, as over 80% of the 955 clusters with $N_{200} > 30$ are detected at at least the $1\sigma$ level. Furthermore, the fits are not sensitive to the precise richness cutoff chosen.

To calculate the $L_X$ for each of these often marginally-detected clusters, we use a procedure based on the count-rate to flux conversion method from the REFLEX survey (Böhringer et al. 2004). First, we calculate the 0.5-2.0 keV (ROSAT hard channel) count rate in a $750\,h^{-1}$ kpc aperture; the fixed aperture was used because it results in better signal-to-noise than a larger scaled aperture (where we only see significant signal in the stacked profiles). The local background is calculated in a $20' - 40'$ annulus using the sector-rejection method of Böhringer et al. (2000).

In REFLEX the temperature is estimated in an iterative fashion from the luminosity, using the $L_X$–$T_X$ relation of Markevitch (1998). As most of the maxBCG clusters do not have a significant flux (or luminosity) measurement, we cannot calculate the individual cluster temperatures in this way. Instead, each cluster temperature is approximated by the stacked spectral temperature from the appropriate richness bin, as shown in Table 4.

This ensures that our stacked cluster luminosities and individual luminosity estimates are on approximately the same footing. Perhaps more importantly, changing the temperature does not change the 0.1-2.4 keV luminosities significantly (e.g. Mohr et al. 1999). This is simply another example of how measuring temperatures with ROSAT is challenging.

The 0.5-2.0 keV count rate is then converted to 0.1-2.4 keV luminosity using Table 2 from Böhringer et al. (2004) with the equivalent hydrogen column density at the position of the cluster (Dickey & Lockman 1990). After converting to luminosity, a $k$-correction is applied using Equation 4 from Stanek et al. (2006), which is a good approximation of Table 3 in Böhringer et al. (2004).[15] The $k$-corrections are not very large, at most 10%.

We compared our method of calculating $L_X$ for individual clusters to the $L_X$ values obtained in the NORAS catalog (see Section 4.2 for details on the X-ray catalog matching). For the matched clusters the values are all consistent within errors with $\sim 10\%$ scatter, and a systematic offset of $< 5\%$. The primary difference in our calculations is that the NORAS fluxes were calculated in an aperture obtained via growth curve analysis (GCA) designed to obtain the best signal-to-noise for each cluster, while we use a fixed physical aperture. Therefore, our fixed temperature and aperture provide an unbiased estimate of the cluster flux and luminosity even without *a priori* knowledge of extended cluster emission. Individual cluster $L_X$ and $N_{200}$ values are shown in Figure 7.

We use `linmix_err` to estimate the power-law slope, normalization, and intrinsic scatter of the underlying distribution of the $L_X$–$N_{200}$ relationship for the 955 richest clusters with $N_{200} \geq 30$. The best fit relation is:

$$\widetilde{L}_X(< 750\,h^{-1}\,\text{kpc}) = e^{3.40\pm0.04}\left(\frac{N_{200}}{40}\right)^{1.61\pm0.13}10^{42}\,h^{-2}\,\text{ergs s}^{-1},$$
$$(5)$$

with an intrinsic scatter $\sigma_{\ln L} = 0.86\pm0.03$. The individual $L_X$ values are calculated within a fixed $750\,h^{-1}$ kpc aperture, and thus this is to be compared to Equation 2. We test the robustness of this result by both splitting the input data into multiple independently fit subsamples and changing the richness threshold slightly. We find that the constraint on the scatter is robust, and the error bar is accurate. Possible systematic biases in the constraint on $\sigma_{\ln L}$ are discussed in Section 5.6.

The scatter-corrected $\widetilde{L}_X$–$\bar{N}_{200}$ relation is shown in Figure 7. The luminosities for the individual $1\sigma$ detections are plotted as solid circles, and the $1\sigma$ upper limits are plotted as empty circles. The typical error bar for detections is shown in the lower-right corner. Contours showing the $\pm1\sigma$ contours on the best-fit median relation are shown in dark gray, and the dashed (dotted) lines show the $\pm1\sigma_{\ln L}$ ($\pm2\sigma_{\ln L}$) scatter constraints. The median relation as constrained by `linmix_err` has been converted to the equivalent mean relation by multiplying the normalization by $\exp(\sigma_{\ln L}^2/2)$, and is shown in light gray. The mean relation agrees well with the individual stacked bins (squares), which are about $\sim 30\%$ brighter

---

[15] Note that there is a typographical error in Equation 4 of Stanek et al. (2006), so that it should read $k(z,T) = \{1 + [1 + \log_{10}(T/5\,\text{keV})]z\}^{1/2}$.
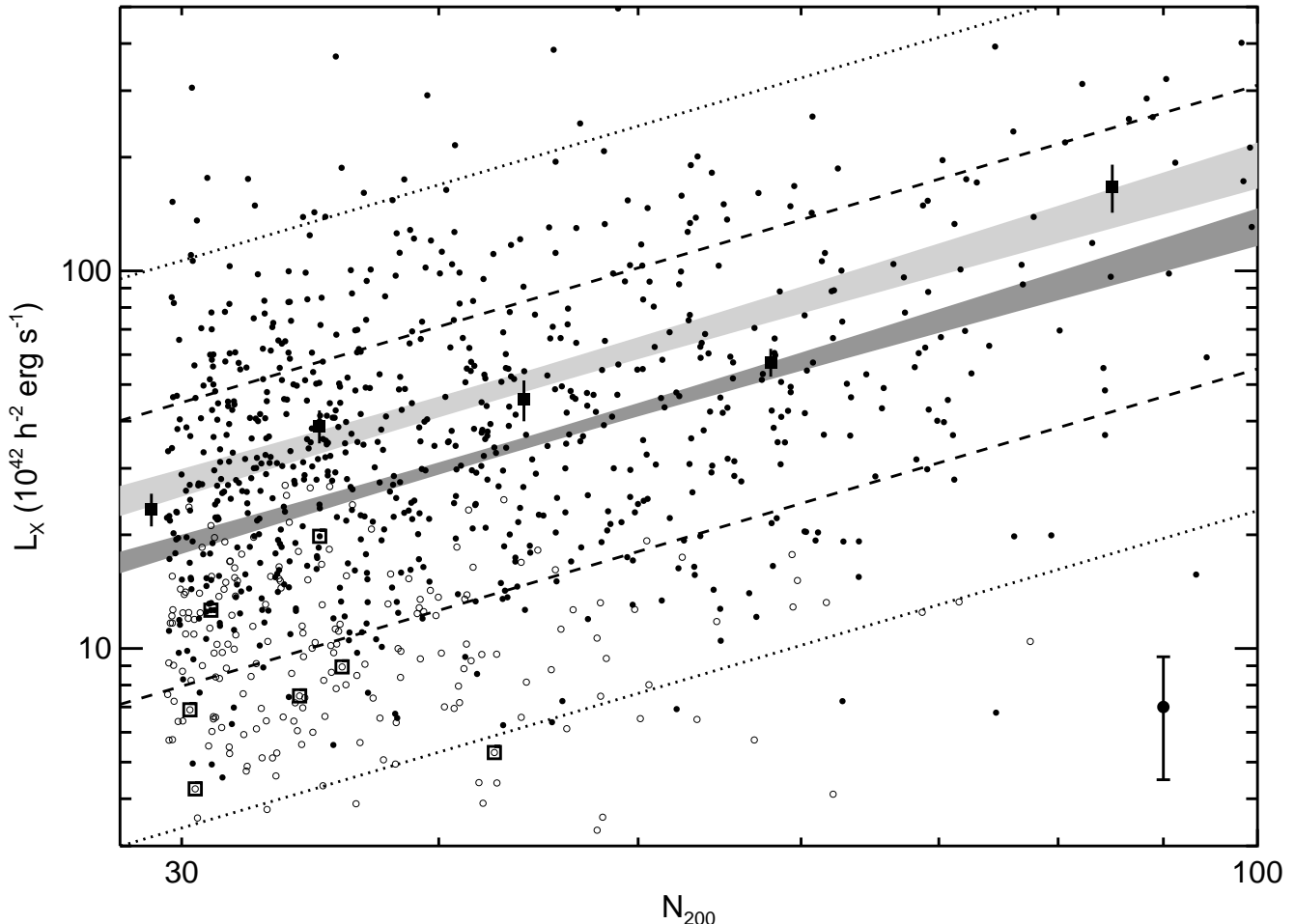
FIG. 7.— $L_X$ vs. $N_{200}$ for individual clusters with $N_{200} \geq 30$. The typical error bar is plotted on the fictitious data point in the lower-right corner. Contours showing the $\pm 1\sigma$ contours on the best-fit median relation are shown in dark gray. The dashed (dotted) lines show the $\pm 1\sigma_{\ln L}$ ($\pm 2\sigma_{\ln L}$) scatter constraints. The median relation as constrained by linmix_err has been converted to the equivalent mean relation by multiplying the normalization by $\exp(\sigma_{\ln L}^2/2)$, and is shown in light gray. The mean relation agrees well with the individual stacked bins (solid squares), which are about $\sim 30\%$ brighter than the underlying median values. The empty squares denote "Abell X-Ray Underluminous" (AXU) clusters (Popesso et al. 2007), which have X-ray luminosities consistent with the observed scatter.

than the underlying median values.

We must emphasize that we are measuring the *observed* scatter in the $L_X$–$N_{200}$ relation as is appropriate to our catalog and stacking method. This scatter comes about not only due to intrinsic $L_X$ variations between the clusters (including different morphologies and merging clusters), but is also due to point sources, cooling flows, and the projection of multiple clusters along the line of sight. For the $\sim 1000$ richest clusters ($N_{200} \geq 30$) used in this exercise, the chance of projection is very low. We do not have any way to remove point sources or bright cool cores from individual clusters in an unbiased way. Operationally, it is not relevant to our measurement whether the scatter is due to intrinsic $L_X$ variations or due to point source and cool-core contamination. To constrain the observed scatter, we need only assume that the underlying distribution is approximately log-normal, which is consistent with our observations.

Gilbank et al. (2004) measure the observed scatter in the $L_X$–$B_{\rm gc}$ relation, where $B_{\rm gc}$ is a richness measure from the amplitude of galaxy-cluster correlation function (Yee & López-Cruz 1999). They use 290 optically-selected clusters, of which 40 have significant detections in $ROSAT$/PSPC observations. Using a Bayesian maximum-likelihood fitting technique, they find a significant correlation between $L_X$ (bolometric) and $B_{\rm gc}$, with a power-law slope of $\sim 1.6$ and an intrinsic scatter of $\sim 50\%$. It must be noted that they introduce a prior weighting, $P_{\rm prior}(\sigma_{\ln L}) \propto 1/\sigma_{\ln L}$, which gives more weight to models with lower scatter. Again, it is difficult to directly compare our measurement of the slope and scatter to the Gilbank et al. (2004) measurements, due to different richness quantities and selection functions.

A large intrinsic scatter in the $L_X$–$N_{200}$ relation can account for optically-selected clusters that appear "underluminous" in X-rays as compared to their optical richness (e.g. Bower et al. 1994, 1997; Donahue et al. 2002; Ledlow et al. 2003; Basilakos et al. 2004; Gilbank et al. 2004; Popesso et al. 2007). In particular, Popesso et al. (2007) present a set of "Abell X-ray Underluminous"

(AXU) clusters with masses determined from velocity dispersion measurements, that are significantly dimmer in X-rays than expected. In Figure 7 the seven AXU clusters that match to maxBCG ($0.1 < z < 0.3$, $N_{200} > 30$) are denoted with open squares. These are all significantly dimmer than the mean $L_X$–$N_{200}$ relation, but are fully consistent with the observed scatter. Velocity dispersion measurements of maxBCG clusters (B07) and comparisons to simulations (Rozo et al. 2007b) have shown that there is considerable mass-mixing in a given $N_{200}$ bin. The low-luminosity clusters could be from lower-mass halos that are picked up as moderate richness in the cluster finder. However, Popesso et al. (2007) argue that the AXU clusters have low $L_X$ relative to their mass. This could be due to biases in masses calculated from velocity dispersions with small samples (e.g. Biviano et al. 2006), or to large intrinsic scatter in the $L_X$–$M_{200}$ relation (e.g. Stanek et al. 2006). Each of these possibilities (or a combination of the two) are consistent with the observations. We further explore the $L_X$–$M_{200}$ relation of maxBCG clusters in a companion letter (Rykoff et al. 2007).

We have reason to believe that the scatter is not fixed as a function of richness. For example, B07 find a significantly larger scatter in the velocity dispersion-richness ($\exp(\overline{\ln \sigma})$–$\bar{N}_{200}$) relation at low richness compared to high richness. However, the quality of our data for this exercise is not adequate to constrain the change in the scatter as a function of richness. Therefore, for the remainder of the paper we adopt this nominal value of $\sigma_{\ln L} = 0.86 \pm 0.03$ to correct the stacked (mean) $\bar{L}_X$ to obtain the true underlying median $\widetilde{L}_X$ values. This essentially requires us to multiply all $\bar{L}_X$ values by a factor of $0.69 \pm 0.02$.

## 4.2. *Comparison to X-Ray Selected Clusters*

We can compare the $\widetilde{L}_X$–$\bar{N}_{200}$ relation for optically-selected maxBCG clusters to that from X-ray selected clusters from the literature. For this exercise we chose to compare to the NORAS (Böhringer et al. 2000) and 400 square degree (400d: Burenin et al. 2006) catalogs, both constructed from ROSAT data, and thus measured in the same energy range as used in this work. The NORAS catalog is an X-ray flux limited cluster catalog constructed from the RASS photon maps in the northern sky. Although it is known to be only $\sim 50\%$ complete, it provides a large sample of bright X-ray clusters that overlap the maxBCG survey region. The 400d catalog is a serendipitous X-ray flux limited cluster catalog constructed from pointed ROSAT PSPC observations. The 400d catalog covers fields sampled from the whole sky, and thus only $\sim 50\%$ of the catalog overlaps the maxBCG survey region.

Our intention in this exercise is to obtain a baseline comparison of the X-ray and optical richness properties of X-ray selected clusters to optically-selected clusters. A somewhat different comparison of NORAS and maxBCG, focused on testing the completeness of maxBCG, was performed in Koester et al. (2007a).

To obtain a list of clean matches between NORAS or 400d clusters and maxBCG clusters, we require that the X-ray position and BCG position be matched within $250\,h^{-1}$ kpc, and the redshift difference to be less than

0.05. This ensures both that the probability of a false match is $\ll 1$ and that we are not selecting, e.g., merging clusters where the X-ray and optical catalogs might utilize different deblending schemes. There are 89 NORAS clusters that match maxBCG, with a median redshift of $\tilde{z} = 0.18$, and 53 400d clusters that match maxBCG, with a median redshift of $\tilde{z} = 0.16$. We convert all X-ray luminosities to 0.1-2.4 keV in the rest frame with our adopted cosmology. Note that the $L_X$ values obtained in NORAS and 400d have been corrected for aperture effects. However, with the adopted $\beta$ parameters ($\beta = 2/3$ for NORAS, and $\beta > 0.6$ for 400d) these corrections produce at most a $\sim 10\%$ offset in $L_X$ compared to the luminosities obtained in our scaled $R_{200}$ apertures.

Figure 8 shows $L_X$ vs. $N_{200}$ for the X-ray selected clusters that meet our matching criteria. The solid circles represent NORAS clusters, and the empty squares represent 400d clusters. The luminosities of the 400d clusters are typically less than that for NORAS due to the deeper flux limit of the pointed ROSAT observations relative to the RASS survey. The dashed line shows the median $\widetilde{L}_X$–$\bar{N}_{200}$ relation, and the dotted lines show the $\pm 1\sigma_{\ln L}$ scatter constraints. It is not surprising to note that X-ray selection picks out primarily the X-ray brightest clusters at a given richness; nearly all the NORAS clusters lie above the median maxBCG relation. The deeper 400d survey selects a sample more representative of the optically-selected clusters, though it is still biased high. Comparison to Figure 7 is instructive. At every richness, the typical X-ray emission from clusters is significantly below what you might expect from X-ray selected catalogs. While this is true for both catalogs, it is especially apparent for NORAS clusters. Although the 400d survey has the sensitivity to detect the richest X-ray dim clusters (as in the lower-right corner of Figure 7), these clusters are quite rare. The limited overlap between the 400d survey region and the maxBCG survey region means that it is very unlikely that the 400d survey would contain one of these specific maxBCG clusters.

## 5. BIASES IN THE $\widetilde{L}_X$–$\bar{N}_{200}$ RELATION

There are a variety of systematic effects which may bias the $\widetilde{L}_X$–$\bar{N}_{200}$ relation. In this section we address six: photometric redshift uncertainty, cluster centering errors, richness variation with redshift, BCG luminosity, point source contamination, and cool core clusters.

## 5.1. *Photometric Redshift Uncertainty*

The maxBCG cluster catalog is based on photometric data, and thus we only have photometric redshifts ("photo-$z$s") for each of the clusters. While the photo-$z$s are relatively precise ($\Delta_z \leq 0.015$), we must investigate how using photometric redshift estimates might bias our stacking results.

If a cluster is actually closer than its photometric redshift would suggest, it will be over-weighted in the stacking analysis. When it is more distant than it seems, it will be underweighted. Even if the photo-$z$ errors are perfectly symmetric, the weighting factor, $w(z) = (d_L(z)/d_L(\tilde{z}))^2$, is not. As a result, uncertainty in photo-$z$ can introduce a bias in the luminosities. This bias can become significant if the photo-$z$ errors are large. The net impact of this effect is to make the clusters appear more luminous than they truly are.
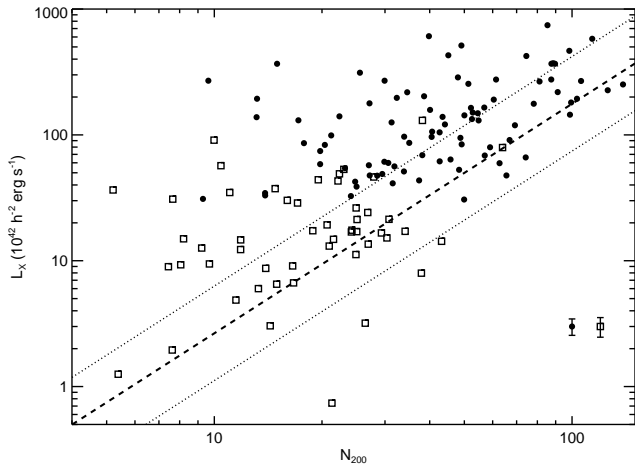
FIG. 8.— $L_X$ vs. $N_{200}$ for X-ray selected clusters that match the maxBCG catalog within $250\,h^{-1}$ kpc. The 89 NORAS clusters (solid circles) are from a flux-limited survey using RASS, and the 53 400d clusters (empty squares) are from a deeper flux-limited survey using $ROSAT$/PSPC pointed observations. The dashed line shows the median $\widetilde{L}_X$–$\bar{N}_{200}$ relation, and the dotted lines show the $\pm 1\sigma_{\ln L}$ scatter constraints. As seen in Figure 7 there is significant scatter in the $L_X$–$N_{200}$ relation. The X-ray selected clusters, especially from NORAS, tend to sample the brightest tail of the distribution at a given richness.

There is also a small volume effect caused by photo-$z$ errors. At a fixed redshift $z$ there is a larger physical volume at a larger distance $z + \delta z$ than at a smaller distance $z - \delta z$. Because of this, more clusters are available at high redshift to scatter low than at low redshift to scatter high. This is similar to Malmquist bias. As above, this effect will cause us to overestimate the cluster luminosities.

We run a Monte Carlo simulation to estimate the combined photo-$z$ bias as a function of richness. Around 37% of the BCGs in the maxBCG catalog used in this analysis have spectroscopic redshifts from the SDSS DR5 spectroscopic catalog (Strauss et al. 2002; Eisenstein et al. 2001). With the spectroscopic subsample, we measure the photo-$z$ offset ($\delta z = z_{ph} - z_{spec}$) distribution in each richness bin and three redshift bins. A Monte Carlo is performed to estimate the overall bias in the measured luminosity by comparing the "true" luminosities convolved with the $\delta z$ distribution to the "observed" luminosities at the measured photometric redshifts.

We find that the overall bias is small ($< 6\%$ at 99% confidence limit), with the observed luminosities slightly overestimating the true luminosities. This bias factor does not vary with richness. We neglect this correction factor due to its small magnitude.

## 5.2. *Centering Biases*

In our stacking exercise, we chose the BCG as the center of the cluster. For many clusters with individual X-ray observations and a bright BCG, this is coincident with the X-ray center. However, there are several types of clusters in which the BCG is not consistent with the center of the X-ray emission. These include merging clusters with disturbed morphologies; clusters without a dominant central galaxy for unambiguous detection by

the maxBCG algorithm; and a few ($\sim 5$) previously identified strong cooling flow clusters. The central galaxies in these clusters host bright AGN and exhibit strong star formation, moving their colors off the red sequence and excluding them from the maxBCG cluster finding algorithm.

We do not expect centering biases to be a significant problem for our calculation of the mean X-ray luminosity for the following reasons. First, the X-ray luminosity is proportional to the electron density $\rho^2$, and thus most of the luminosity comes from the central region. With our large apertures ($> 750\,h^{-1}$ kpc) as long as the core of a cluster is within the aperture, the photon counting exercise will include most of the cluster photons. Second, we have reason to believe from simulations that most of the richer clusters are well centered (J07). This is not to say that the cluster centering will not have any effect: as shown in Section 3.3, the $\beta$-model parameter is highly dependent on the centering distribution.

To confirm this, we perform some simple tests of de-centering the clusters. If we randomly offset all the cluster positions with a 2D Gaussian with an rms of $300\,h^{-1}$ kpc (comparable to the centering distribution modeled in J07), the mean $\bar{L}_X$ values decrease by $< 10\%$, and less than $1\sigma$. This rms value was chosen because, as is seen in Figure 4, the vast majority of the X-ray cluster matches are within $250\,h^{-1}$ kpc. Therefore, we do not consider cluster miscentering to contribute a significant bias to our X-ray luminosity calculation.

## 5.3. *Richness Variation with Redshift*

We investigate whether the observed $\bar{L}_X$ at fixed richness changes with redshift. Modest evolution in $\bar{L}_X$ at fixed *mass* is expected. If the clusters are evolving in a self-similar manner, then we expect the higher redshift clusters to be more luminous than the lower redshift clusters, due to the fact that the Universe was more dense at higher redshift. The expectation is that $L_X \propto \rho_c(z)^{7/6}$, where $\rho_c$ is the critical density of the Universe at redshift $z$ (Kaiser 1986). Therefore, clusters at a given *mass* at a redshift $z = 0.3$ should be $\sim 30\%$ brighter than similar clusters at a redshift of $z = 0.1$.

To study possible variation of $\bar{L}_X$ at fixed richness, we split the cluster sample into three redshift bins, containing the bottom 25%, middle 50%, and top 25% of clusters in our sample. The low redshift bin ranges from $0.10 < z < 0.17$ with a median redshift of $\tilde{z} = 0.14$; the middle redshift bin ranges from $0.17 < z < 0.26$ with a median redshift of $\tilde{z} = 0.23$; and the high redshift bin ranges from $0.26 < z < 0.30$ with a median of $\tilde{z} = 0.28$. To obtain increased signal-to-noise in these bins, we combine richness bins $41 \leq N_{200} \leq 50$ and $51 \leq N_{200} \leq 70$; $26 \leq N_{200} \leq 32$ and $33 \leq N_{200} \leq 40$; and $18 \leq N_{200} \leq 20$ and $21 \leq N_{200} \leq 25$. These wider bins are the same that were used in the lensing analysis of S07.

Figure 9 shows the stacked $\bar{L}_X$ as a function of $\bar{N}_{200}$ for the three different richness bins. The dashed line shows the mean relation (Equation 1) for all clusters from Section 4. The high redshift clusters (diamonds) are significantly more luminous than the low redshift clusters (circles). We parameterize the variation with a factor of $(1 + z)^\gamma$, and fit all the redshift and richness bins simul-
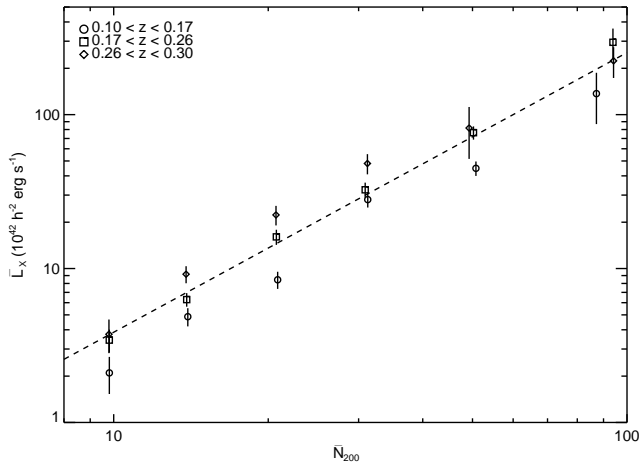
FIG. 9.— Mean $\bar{L}_X$–$\bar{N}_{200}$ in three redshift bins, calculated within the scaled $R_{200}$ apertures. The high redshift bin (diamonds) are significantly more luminous than the low richness bin (circles), indicating significant variation in the $\bar{L}_X$–$\bar{N}_{200}$ relation with richness. The dashed line is the stacked mean relation from Equation 1, which is consistent with the mean relation for the central redshift bin (squares).

taneously with a model of the form:

$$\bar{L}_X(< R_{200}) = e^{\alpha} \left( \frac{\bar{N}_{200}}{40} \right)^{\beta} \left( \frac{1+z}{1+\tilde{z}} \right)^{\gamma} 10^{42} \, h^{-2} \, \mathrm{ergs \, s^{-1}},$$
(6)

where $\tilde{z} = 0.23$, the median redshift of the cluster catalog. This results in a good fit ($\chi^2/\nu = 18.4/15$) with the best-fit parameters: $\alpha = 3.90 \pm 0.04$; $\beta = 1.85 \pm 0.05$; $\gamma = 6.0 \pm 0.8$. Note that $\alpha$ and $\beta$ are consistent with the mean relation in Equation 1. The redshift variation parameter, $\gamma$, is quite large, and shows that the high redshift bin ($\tilde{z} = 0.28$) is almost twice as bright as the low redshift bin ($\tilde{z} = 0.14$). This is significantly in excess of the self-similar prediction. The challenge is to determine the origin of this redshift dependent shift in $\bar{L}_X$ at fixed richness.

The photo-$z$ errors described in Section 5.1 may account for some of this effect. Although the absolute photo-$z$ errors are better than 0.015 at all redshifts, the *relative* photo-$z$ errors are larger at low redshift than at high. Therefore, the impact of photo-$z$ bias is larger at low redshift than at high redshift. We repeated the Monte Carlo simulation described in Section 5.1 to measure the photo-$z$ bias from each redshift bin. The additional redshift bias is $< 10\%$ (99% confidence limit) in the low redshift bin, and $< 2\%$ (99% confidence limit) in the high redshift bin. The photo-$z$ bias therefore remains smaller than the observed variation in $L_X$, although the effect is in the same sense as the variation we observe, and is a contributing factor.

A more likely possibility is redshift dependent variation of $N_{200}$ at fixed mass. If our high redshift clusters have systematically smaller $N_{200}$ at fixed mass, this would have the effect of shifting the high redshift points in Figure 9 to the left. After assuming self-similar evolution and that $N_{200}$ is a good mass proxy (S07, J07), we re-fit the data to Equation 6 to calculate the excess variation in the $L_X$–$N_{200}$ relation that might be due to variation of

$N_{200}$ at fixed mass. This results in a best-fit $\gamma = 4.5 \pm 0.8$, implying a fractional decrease in $N_{200}$ of 30%–40% from our lowest redshift bin ($\tilde{z} = 0.14$) to our highest redshift bin ($\tilde{z} = 0.28$). This is consistent with the redshift dependent variation in the velocity dispersion–optical richness relation measured by B07. However, we must note that redshift dependence in the observed lensing shear, $\Delta\Sigma$, is significantly smaller (S07). Unfortunately, none of these approaches is yet able to confidently determine the nature of the observed variation. For example, this effect could be caused by incorrect handling of the $0.4 \, L_*$ and color cuts that determine which galaxies are included in the richness estimate. It might also be "true" evolution, such that clusters have fewer red-sequence galaxies brighter than $0.4 \, L_*$ at fixed mass at higher redshifts. Further work, including improving the richness estimates, is in progress to constrain the nature of this evolution.

### 5.4. *BCG Luminosity*

We now investigate the effect BCG $i$-band luminosity ($L_{\mathrm{BCG}}$, see Koester et al. (2007a) for details) has on the mean X-ray luminosity $\bar{L}_X$. Simulations and semi-analytical modeling predict that dark matter halos formed at early times have brighter BCGs and lower richness than those which form late (Zentner et al. 2005; Wechsler et al. 2006; Croton et al. 2007). Thus, we expect that the X-ray luminosity should be correlated with $L_{\mathrm{BCG}}$ at fixed richness. Furthermore, optical and X-ray observations of individual nearby clusters show that more luminous BCGs are correlated with more massive halos with higher X-ray temperature and luminosity (e.g. Lin & Mohr 2004). This trend has already been seen in the mean velocity dispersion analysis of maxBCG clusters, as the clusters with more luminous BCGs had significantly larger velocity dispersions than clusters with similar richness (B07).

In an exercise similar to that performed in the previous section, we split each wide richness bin into three bins of $L_{\mathrm{BCG}}$. As $L_{\mathrm{BCG}}$, unlike redshift, is correlated with $N_{200}$, we are unable to use the same $L_{\mathrm{BCG}}$ split for each $N_{200}$ bin. Therefore, we sort the clusters in each richness bin by $L_{\mathrm{BCG}}$, and split the sample into the top 25%, middle 50%, and bottom 25%, and then restack. The results are shown in Figure 10. It is readily apparent that the clusters with the most luminous BCG in a given richness bin (diamonds) are significantly more luminous in X-rays than other clusters in the bin. This effect is most dramatic at lower richnesses. This is expected, as the BCG is more dominant in low richness clusters than high richness clusters (e.g. Lin & Mohr 2004). It is also notable that there does not appear to be a significant difference between the $\bar{L}_X$ for the low $L_{\mathrm{BCG}}$ and middle $L_{\mathrm{BCG}}$ bins.

We parameterize the effect of $L_{\mathrm{BCG}}$ on $\bar{L}_X$ using a similar procedure as performed for the redshift variation. The richness and $L_{\mathrm{BCG}}$ bins are fit simultaneously with a model of the form:

$$\bar{L}_X(< R_{200}) = e^{\alpha} \left( \frac{\bar{N}_{200}}{40} \right)^{\beta} \left( \frac{\bar{L}_{\mathrm{BCG}}}{10^{11} \, L_{\odot}} \right)^{\eta} 10^{42} \, h^{-2} \, \mathrm{ergs \, s^{-1}}.$$
(7)

This results in an adequate fit ($\chi^2/\nu = 25.9/15$) with the best-fit parameters: $\alpha = 3.86 \pm 0.04$; $\beta = 1.50 \pm 0.06$;
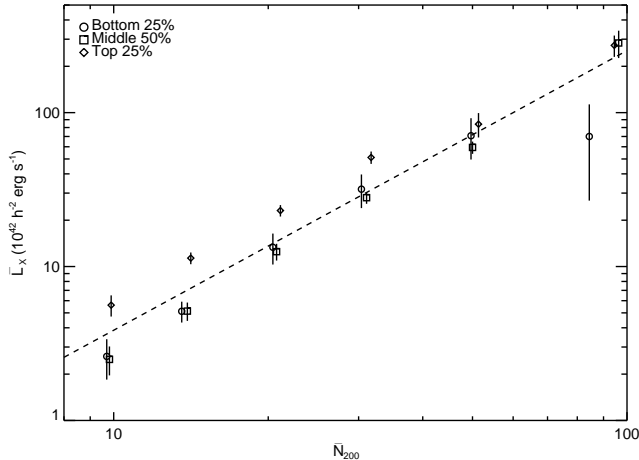
FIG. 10.— Mean $\bar{L}_X$–$\bar{N}_{200}$ (within the scaled $R_{200}$ apertures) split according to BCG luminosity. Each $N_{200}$ bin has been sorted by the optical luminosity of the BCG ($L_{\mathrm{BCG}}$) of each cluster in the bin. The stacking exercise has been performed on the top 25% (diamonds); middle 50% (squares); and bottom 25% (circles). Note that $L_{\mathrm{BCG}}$ is correlated with $N_{200}$, and thus the $L_{\mathrm{BCG}}$ splits are different for each $N_{200}$ bin. The dashed line shows the mean relation for all the clusters from Equation 1. The clusters with the most luminous BCGs also tend to be the most luminous in X-rays. This effect is strongest at low richness, where the BCG is a larger fraction of the total optical luminosity of the cluster.

$\eta = 0.82 \pm 0.10$. Although the normalization is the same as in Equation 1, the slope is significantly more shallow. This is caused by the correlation between $L_{\mathrm{BCG}}$ and $N_{200}$. After taking this into account, the mean relation shown here is fully consistent with that calculated without splitting the bins by $L_{\mathrm{BCG}}$. The reason the $\chi^2$ of the fit is relatively high is because it does not appear that $\bar{L}_X$ is smooth function of $\bar{L}_{\mathrm{BCG}}$: the effect of $L_{\mathrm{BCG}}$ is not symmetric, and only tends to boost the X-ray luminosity of clusters with relatively bright BCGs.

It is not entirely clear whether this effect is due to an imperfect cluster finder, our crude richness definition, or due to real cluster physics. Clusters with brighter, more dominant BCGs are more likely to be correctly centered and thus might be more luminous in X-rays. However, as we showed in Section 5.2, the effect of decentered clusters on $\bar{L}_X$ is much smaller than the effect we see due to $L_{\mathrm{BCG}}$. Meanwhile, our richness definition, $N_{200}$, is a count of red-sequence galaxies brighter than $0.4\,L_*$. It is thus not surprising that a poor cluster with an exceptionally bright BCG might be more massive and more X-ray luminous than a cluster at a similar richness with a more typical BCG. Finally, it is possible that these clusters are associated with halos that formed early, allowing many of their member galaxies to merge into a very large BCG (Zentner et al. 2005; Wechsler et al. 2006; Croton et al. 2007). Deeper targeted X-ray observations of specific clusters will be required to determine if we can use $L_{\mathrm{BCG}}$ and other optical properties to constrain the age of its dark matter halo.

### 5.5. *Point Source Contamination*

When calculating the projected X-ray luminosity from the hot intracluster medium, there is the possibility of contamination due to X-ray point sources. Some point sources, such as cluster AGN, are associated with the cluster, but in general their luminosities are not tightly correlated with that of the ICM. Other point sources that are chance coincidences, such as foreground stars and background quasars, might also boost the apparent luminosity. The problem of point source contamination is exacerbated by the broad PSF of the RASS survey. Due to the large PSF, it is difficult to accurately excise point sources from the higher redshift clusters, even when their positions are known. For the stacking exercise, foreground and background sources are not a significant problem. Assuming the positions of these point sources are uncorrelated with the cluster positions, the contribution from these sources is subtracted with the background estimation, as is demonstrated by our stack of random points in Figure 1. At the same time, these point sources, both those associated with the clusters and those that are chance projections, may increase the observed scatter. In general, we note that $L_X$ values calculated from RASS are not corrected for point source contamination (e.g. Böhringer et al. 2000, 2004). We wish to perform a first-order check on possible contamination from cluster AGN, the dominating point sources that might bias the observed $\bar{L}_X$.

Martini et al. (2007) have recently performed a detailed survey of the distribution of AGN in galaxy clusters for eight moderate redshift clusters, comparable to the redshift range of the maxBCG catalog. They find that moderately bright AGN ($L_X > 10^{42}\,\mathrm{erg\,s^{-1}}$) associated with bright cluster members ($\gtrsim 0.5\,L_*$) make up around $\sim 1\%$ of the total cluster member population. This implies that many of the richest maxBCG clusters contain at least one moderately bright AGN. These clusters have an extremely bright ICM ($\bar{L}_X \sim 10^{44}\,h^{-2}\,\mathrm{ergs\,s^{-1}}$), and thus the fraction of the luminosity from cluster AGN will, on average, be very small. If we extrapolate the same AGN fraction to our poorest clusters ($N_{200} \sim 10$, perhaps one in ten will host a moderately bright AGN. Although these AGN might have a luminosity comparable to the ICM for these 10% of poor clusters, this small fraction should not strongly bias the stacked average.

As a simple check for contamination in the X-ray signal from cluster AGN, we match maxBCG cluster member galaxies to radio sources from the FIRST survey (White et al. 1997). The FIRST survey covers approximately the same footprint as the SDSS, down to a typical flux limit of $1\,\mathrm{mJy}$ at $1.4\,\mathrm{GHz}$. Using $1.4\,\mathrm{GHz}$ radio detections as a proxy for AGN activity has the advantage that the radio spectrum is often flat, and thus the $1.4\,\mathrm{GHz}$ flux is not a strong function of redshift. The disadvantages are that only 10% of X-ray bright quasars and AGN are radio loud, and that there is a large scatter between X-ray and radio luminosities of these objects. For example, Martini et al. (2007) noted that for the same small set of clusters none of the X-ray selected AGN are radio loud Morrison et al. (2003).

Although we have an incomplete selection function, we can still constrain the contamination from cluster AGN. If the mean $\bar{L}_X$ is significantly boosted by cluster AGN, then we would expect the clusters which match radio sources to be relatively bright. This effect would be greatest at low richness and low $\bar{L}_X$ when the ICM is not as hot or bright. For each richness bin, we matched the maxBCG cluster members within $750\,h^{-1}\,\mathrm{kpc}$ of the

TABLE 5. RADIO SOURCE MAXBCG MEMBER MATCHES

| Richness Range | Clusters w/ Radio Sources | % Clusters w/ Radio Sources |
|---|---|---|
| $71 \leq N_{200} \leq 188$ | 45 | 82% |
| $51 \leq N_{200} \leq 70$ | 91 | 65% |
| $41 \leq N_{200} \leq 50$ | 125 | 62% |
| $33 \leq N_{200} \leq 40$ | 183 | 54% |
| $26 \leq N_{200} \leq 32$ | 284 | 45% |
| $21 \leq N_{200} \leq 25$ | 420 | 37% |
| $18 \leq N_{200} \leq 20$ | 332 | 30% |
| $12 \leq N_{200} \leq 17$ | 1330 | 25% |
| $9 \leq N_{200} \leq 11$ | 1341 | 18% |



FIG. 11.— Histograms of the distribution of $\bar{L}_X$ values obtained from resampling the same number of clusters which match FIRST radio sources (as a proxy for AGN contamination) in each bin. The vertical dashed lines indicate $\bar{L}_X$ for the clusters which match radio sources. The clusters with radio matches are not significantly more luminous than those drawn from the distribution, except for the $12 \leq N_{200} \leq 17$ bin (discussed in the text). This would indicate that, on average, AGN emission is not biasing our stacked $\bar{L}_X$ values.

BCG to sources in the FIRST survey. Table 5 shows the number of clusters in each bin that have members matched with the FIRST catalog. More detailed work is in progress in cross-correlating the maxBCG catalog with radio sources to explore cluster AGN feedback and related issues (see also Croft et al. (2007)).

We wish to compare how the radio selected subset of clusters compares to a randomly selected subset of clusters of similar richness. In each richness bin, we ran 10000 trials by sampling (with replacement) from the entire set of clusters in the bin, sampling the same number of clusters that match radio sources. As a quick estimate of the mean luminosity, rather than performing the full stacking analysis and spectral fits, we calculated the stacked and weighted, background-subtracted hard channel (0.5-2.0 keV) counts in a fixed $750\,h^{-1}\,$kpc aperture. The resulting count rate was converted to $\bar{L}_X$ using the method described in Section 4.1. We can then compare the mean $\bar{L}_X$ of the clusters which match radio sources to the typical values of $\bar{L}_X$ that we would expect when drawing that same number of clusters from the entire sample. The results are shown in Figure 11. In each panel the histogram shows the distribution of $\bar{L}_X$ values obtained from the resampling, and the vertical dashed line marks the mean $\bar{L}_X$ of the radio-matched clusters. We do not see any significant bias as a function of richness. The only bin in which the radio matches appear to be outliers is the $12 \leq N_{200} \leq 17$ richness bin. This is due to random chance, in that the clusters in this richness bin with the highest $L_X$ also happen to match radio sources; although there is no obvious indication in the RASS data that there is point source contamination on these clusters, further follow-up with *Chandra* or *XMM/Newton* would be required to clarify this.

### 5.6. *Cool Core Clusters*

There is much evidence that cool core clusters increase the scatter in X-ray cluster properties. By excluding cluster cores in high resolution imaging, many X-ray parameters become more tightly correlated (e.g. O'Hara et al. 2006; Chen et al. 2007; Maughan 2007). The broad ROSAT PSF, combined with the fact that most of our clusters do not have individual X-ray detections, makes it impossible to exclude cluster cores in our stacking analysis. However, a few of the brightest clusters ($> 10^{44}\,h^{-2}\,$ergs s$^{-1}$) at moderate richness ($N_{200} \sim 45$) are well known cool-core clusters. We thus investigate what effect cool core clusters have on our estimate of the
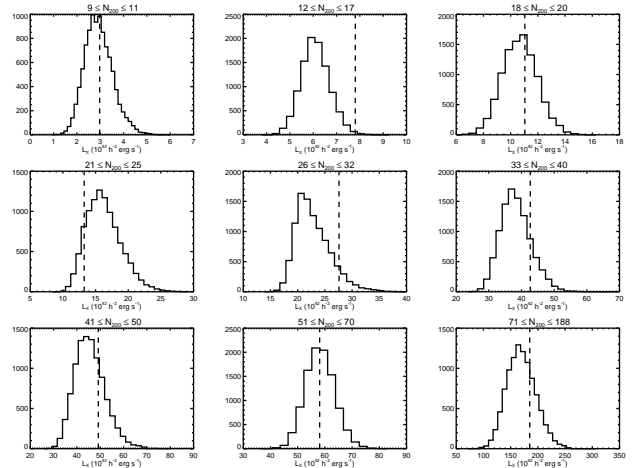
median $\widetilde{L}_X$ and scatter $\sigma_{\ln L}$ in the $\widetilde{L}_X$–$\bar{N}_{200}$ relation.

There does not exist an unbiased volume-limited catalog of cool core X-ray clusters which can be fairly compared to the maxBCG catalog. Peres et al. (1998) used ROSAT pointed observations of an X-ray flux limited catalog (Edge et al. 1990) to estimate the central cooling time of 55 nearby clusters. Two of these clusters are in the maxBCG catalog (A1689, A2244) and exhibit characteristics of a cool core ($t_{cool} < 10\,$Gyr). Bauer et al. (2005) used *Chandra* observations of the higher redshift ($z > 0.15$) BCS clusters to systematically estimate the central cooling time of bright X-ray clusters. We identify 7 maxBCG clusters (A750, A963, A1835, RXJ 2129.6+0005, Z2701, Z3146, Z7160) from this sample with cooling times $t_{cool} < 10\,$Gyr which we mark as cool core clusters. Finally, we identify ClG J1504-0248 (Böhringer et al. 2005) as maxBCG cluster with a cool core. It should be noted that most of these clusters have a moderate richness ($30 < N_{200} < 50$) and are in the brightest tail of the $L_X$ distribution for their richness. Furthermore, the central galaxies of these clusters tend to show strong $H\alpha$ emission in SDSS spectroscopy. In fact, for a few of these clusters the true BCG is not in the list of cluster members because the strong $H\alpha$ emission changes the apparent galaxy color, making it inconsistent with the red-sequence used in the cluster finding algorithm.

After excluding these cool core clusters (which might bias the $\widetilde{L}_X$–$N_{200}$ relation) we recalculate the stacked mean relationship as well as the median relationship with scatter. When calculating the median relationship with scatter, as in Section 4.1, the normalization and slope shift by $\ll 1\sigma$, as these values are not strongly affected by outliers. However, the intrinsic observed scatter decreases to $\sigma_{\ln L} = 0.77 \pm 0.03$, which is a $\sim 2\sigma$ shift. It is not surprising that $\sigma_{\ln L}$ decreases: we are delib-

erately removing the brightest clusters. Meanwhile, the stacked relation is also slightly affected by these bright outliers, and after cutting the known cool core clusters the normalization of the stacked relation decreases by $\sim 1\sigma$. After following the previously described prescription for converting the stacked mean relation to a scatter-corrected median relation, we find that removing the known cool core clusters decreases the normalization by $\lesssim 5\%$. We therefore do not consider that cool core clusters are significantly biasing our relation. We must once again emphasize that the intrinsic scatter we measure is the *observed* scatter that takes into account *all* X-ray observations of the maxBCG clusters, regardless of X-ray morphology of the clusters.

## 6. THE LUMINOSITY–VELOCITY DISPERSION RELATION ($\widetilde{L}_X$–$\widetilde{\sigma}$)

B07 have measured the median velocity dispersion ($\widetilde{\sigma} \equiv \exp(\overline{\ln \sigma})$) as a function of $\bar{N}_{200}$ for the maxBCG catalog. The richness bins used to measure the stacked velocity dispersions, as well as the scatter in the $\sigma$–$N_{200}$ relation, are the same as those used in this work. However, in order to measure velocity dispersions, only clusters that have the BCG and at least one additional member galaxy in the SDSS DR5 spectroscopic subsample (Strauss et al. 2002; Eisenstein et al. 2001) were used. The spectroscopic subsample preferentially selects bright/nearby galaxies, and thus the selection of clusters used in B07 ($\tilde{z} = 0.16$, with $z \geq 0.05$) is slightly different than that for the full maxBCG catalog ($\tilde{z} = 0.23$, with $z \geq 0.1$). As discussed in Section 5.3, the lower redshift clusters have a smaller $\bar{L}_X$ than the higher redshift clusters. We therefore re-run our stacking procedure on exactly those clusters used in B07, and use the known spectroscopic redshifts of the BCGs rather than the photometric redshifts. This ensures that, for this exercise at least, we are not affected by any possible photometric redshift biases, which otherwise could be significant for the nearest clusters ($z < 0.1$) where the relative photo-$z$ error ($\Delta_z/z \gtrsim 15\%$) is quite large. Table 6 shows the richness bins used, as well as the mean $\bar{L}_X$ (this work) and median $\widetilde{\sigma}$ (from B07) for the nine richness bins. The slope of the $\bar{L}_X$–$\bar{N}_{200}$ relation is nearly identical for the spectroscopic subsample as reported in Section 4, but the normalization is lower by 10%, due to the different redshift selection.

We take the mean $\bar{L}_X$ values and corrected them for scatter as described in Section 4.1 to obtain $\widetilde{L}_X$. Figure 12 shows the median $\widetilde{L}_X$–$\widetilde{\sigma}$ relation for maxBCG clusters with richness $N_{200} \geq 9$. Each data point (solid circles) is obtained from the same richness bin and same cluster selection. The dark gray band shows the best-fit relation ($\pm 1\sigma$) from clusters in the spectroscopic subsample of the maxBCG catalog, with the following functional form:

$$\widetilde{L}_X(< R_{200}) = e^{2.73 \pm 0.11} \left( \frac{\widetilde{\sigma}}{500 \,\mathrm{km\,s^{-1}}} \right)^{4.30 \pm 0.43} h^{-2}\,\mathrm{ergs\,s^{-1}}$$

(8)

The scaling relation predicted by self-similar cluster evolution is that $L_X \propto T^2 \propto \sigma^4$ (e.g. Kaiser 1986; Markevitch 1998), which is consistent with our observations. We note that if we could convert our 0.1-2.4 keV luminosities to $L_{X,\mathrm{bolo}}$, this would steepen our relation, as
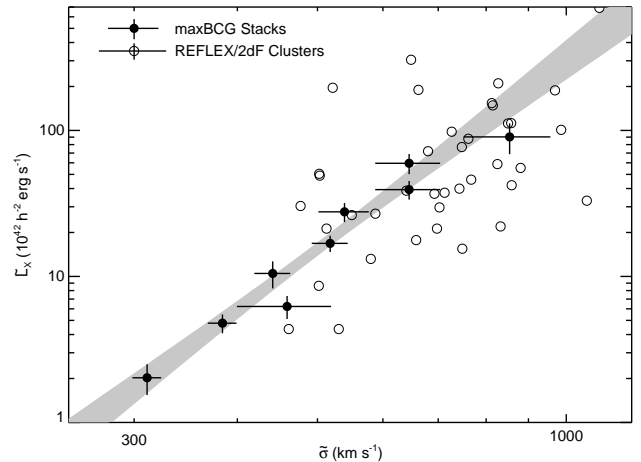


FIG. 12.— Median $\widetilde{L}_X$ vs. $\widetilde{\sigma}$ for the maxBCG clusters. $\widetilde{L}_X$ and $\widetilde{\sigma}$ for each stacked data point (solid circles) is measured in a given richness bin using the cluster selection from B07. The gray band represents the best-fit relation ($\pm 1\sigma$), where $\widetilde{L}_X \propto \widetilde{\sigma}^{4.30 \pm 0.43}$, consistent with self-similar evolution. The empty circles show $L_X$ and $\sigma$ values for individual X-ray selected REFLEX clusters as measured in the 2df survey (Hilton et al. 2005), corrected to the cluster rest frame. The fictitious data point in the legend in the upper left shows the typical errors on these values. The individual X-ray selected clusters have slightly higher ($\sim 1\sigma$) velocity dispersions at a given X-ray luminosity, as compared to the maxBCG stacked measurements.

the clusters with higher velocity dispersions also have a higher temperature and larger $L_{X,\mathrm{bolo}}/L_{X,0.1-2.4}$ ratio. As mentioned previously, such a conversion is not practical for the stacking exercise using ROSAT data. The slope of our 0.1-2.4 keV $\widetilde{L}_X$–$\widetilde{\sigma}$ relation is consistent with that measured for REFLEX clusters (Ortiz-Gil et al. 2004; Hilton et al. 2005).

We compare this median relation to that obtained previously for individual X-ray selected clusters. Hilton et al. (2005) calculated the velocity dispersions of REFLEX clusters by cross-correlating the REFLEX catalog with the Two-degree Field Galaxy Redshift Survey (2dF; Colless et al. 2001). Figure 12 shows 39 individual REFLEX clusters (empty circles) from Hilton, et al. (2007, private communication) after converting the velocity dispersions to the cluster rest frame. In the upper-left corner the empty circle shows the typical errors in 0.1-2.4 keV $L_X$ and $\sigma$ for the REFLEX/2dF clusters. Hilton et al. (2005) found the slope of the X-ray selected $L_X$–$\sigma$ relation to be $4.0 \pm 0.6$, consistent with our observations. However, the individual X-ray selected clusters tend to have a slightly higher ($\sim 1\sigma$) velocity dispersion at a given X-ray luminosity compared to the stacked maxBCG clusters. This is possibly caused by the difficulty in measuring velocity dispersions for individual clusters. Contamination from non-virialized galaxies and interlopers will more likely result in an overestimate of the velocity dispersion rather than an underestimate.

## 7. SUMMARY

By stacking observations from the *ROSAT* All-Sky Survey, we measure the mean X-ray luminosity as a function of richness for optically-selected clusters from the maxBCG catalog. With a large number of clus-

TABLE 6. $\bar{L}_X$ AND $\widetilde{\sigma}$ FOR SPECTROSCOPIC SUBSAMPLE

| Richness Range | $\bar{N}_{200}$ | $R_{200}$ $(h^{-1}\,\mathrm{Mpc})$ | $\bar{L}_X$ $(10^{42}\,h^{-2}\,\mathrm{ergs\,s^{-1}})$ | $\widetilde{\sigma}$ $\mathrm{km\,s^{-1}}$ |
|---|---|---|---|---|
| $71 \leq N_{200} \leq 188$ | 83.9 | 1.69 | $131 \pm 28$ | $854 \pm 103$ |
| $51 \leq N_{200} \leq 70$ | 58.4 | 1.45 | $86.6 \pm 11.4$ | $645 \pm 58$ |
| $41 \leq N_{200} \leq 50$ | 44.7 | 1.32 | $57.2 \pm 6.9$ | $645 \pm 58$ |
| $33 \leq N_{200} \leq 40$ | 35.9 | 1.22 | $40.3 \pm 4.9$ | $539 \pm 38$ |
| $26 \leq N_{200} \leq 32$ | 28.6 | 1.10 | $24.5 \pm 2.5$ | $518 \pm 26$ |
| $21 \leq N_{200} \leq 25$ | 22.7 | 1.02 | $15.2 \pm 2.8$ | $441 \pm 22$ |
| $18 \leq N_{200} \leq 20$ | 19.0 | 0.94 | $9.05 \pm 1.39$ | $459 \pm 60$ |
| $12 \leq N_{200} \leq 17$ | 14.0 | 0.82 | $6.95 \pm 0.84$ | $384 \pm 15$ |
| $9 \leq N_{200} \leq 11$ | 9.9 | 0.73 | $2.94 \pm 0.62$ | $311 \pm 12$ |

ters in each bin, the stacking exercise has the power to probe to much lower flux limits than are possible for X-ray selected surveys. Thus, a highly pure and complete volume-limited catalog with clusters selected by their optical properties can be used to measure the mean $\bar{L}_X$.

We find that $\bar{L}_X$ scales with optical richness, $N_{200}$, with a simple power-law form over two orders of magnitude in $\bar{L}_X$. Our results are similar to those obtained in DKM07 by stacking RASS observations of clusters identified in 2MASS. However, we find that stacked temperature measurements from *ROSAT* are significantly biased for higher temperature clusters. Therefore, we restrict our analysis to luminosities calculated in the 0.1-2.4 keV band rather than extrapolating to calculate bolometric luminosities. Furthermore, we have shown that the $\beta$-model fits to the stacked radial profiles of moderate redshift clusters are dominated by a combination of the broad *ROSAT* PSF and the offset distribution between maxBCG clusters and correlated X-ray sources. On the other hand, calculating X-ray luminosity in the 0.1-2.4 keV band, which relies primarily on counting photons, is not strongly biased by spectral fits or profile fits. As $L_X$ scales with the square of the density, as long as the core of a cluster is within the stacking aperture, we can obtain a high reliability estimate of the mean cluster luminosity.

By measuring the X-ray flux at the positions of individual maxBCG clusters, we are able to constrain the observed scatter in the $L_X$–$N_{200}$ relation. Assuming a log-normal distribution of $L_X$ as a function of $N_{200}$, we find $\sigma_{\ln L} = 0.86 \pm 0.03$. This scatter is quite large, and thus it is necessary to correct for the scatter when calculating the median of the underlying distribution $\widetilde{L}_X$. The richness measure we have used in this work, $N_{200}$, is simply the count of red-sequence galaxies within a scaled $R_{200}$ aperture, but nevertheless is a good proxy for $L_X$ on average. It is likely that improved richness measurements can be made. From the evidence presented here, it seems likely that these new richness estimators will include information about BCG luminosity, and will more carefully control variations in cluster membership with redshift.

The large scatter in the $L_X$–richness relation does have some significant effects on cluster selection. First, X-ray selection with a high flux limit, as with the NORAS catalog, tends to pick out the clusters with the highest $L_X$ at a given richness. Second, the large scatter in the $L_X$–$N_{200}$ relation means that there are a significant number of optically selected clusters that are seemingly "under-luminous". Optically selected clusters will often appear relatively dim compared to X-ray selected clusters at a similar richness.

The goal of cluster selection and identification is to find a low scatter proxy for halo mass. Both X-ray and optical selection techniques suffer from different limitations. X-ray flux limited surveys can only find the brightest X-ray clusters, and are thus limited to a combination of the brightest and nearest clusters. Furthermore, there may be significant scatter between X-ray luminosity and halo mass (Stanek et al. 2006; Nord et al. 2007). Optical surveys such as maxBCG may be volume limited out to moderate redshift, but optical richness also has a large scatter with respect to X-ray luminosity and mass (B07). The development of more precise mass proxies, including $T_X$, the Compton Y parameter (Nagai 2006), $Y_X$ (Kravtsov et al. 2006), and potentially more sophisticated optical richness estimates may allow selection of cluster catalogs more closely approximating the mass-limited catalog we aspire to.

By combining our present analysis with the velocity dispersion measurements of B07, we have measured the median $\widetilde{L}_X$–$\widetilde{\sigma}$ relation for the maxBCG clusters. The relation has a slope of $4.30 \pm 0.43$, consistent with the prediction of self-similar cluster evolution. Previous measurements of the $L_X$–$\sigma$ relation have been complicated by both selection effects and a large scatter, as the derived slope depends strongly on the fitting technique used. By stacking clusters from a volume-limited catalog and correcting for scatter, both $\widetilde{L}_X$ and $\widetilde{\sigma}$ are much better constrained, allowing a robust calculation of the relation. In our analysis, we do not see any evidence of a break in the $\widetilde{L}_X$–$\widetilde{\sigma}$ relation at the poor cluster (group) scale, as has been hinted at previously (e.g. Xue & Wu 2000). This might be due to the fact that the maxBCG cluster finder works with red-sequence clusters, and does not find groups with a large blue galaxy fraction.

We can also compare $\bar{L}_X$ as determined from this method to weak lensing masses determined from the same maxBCG cluster catalog (S07, J07). Determining the true $L_X$–$M_{200}$ relation is not only important for understanding cluster physics, but for calibrating the selection function of X-ray clusters used as cosmological probes (e.g. Stanek et al. 2006). We have made this measurement in a companion letter (Rykoff et al. 2007). In addition, the comparison of the X-ray luminosities, weak lensing masses, and velocity dispersions can be used

in conjunction with the number function of maxBCG clusters to constrain cosmological parameters (e.g. Rozo et al. 2007b). This work is ongoing.

Refined measurements of the scatter, point source contamination, and confirmation of catalog purity will require deeper pointed X-ray observations. We are currently investigating serendipitous maxBCG cluster observations by deeper pointed *ROSAT*/PSPC observations, as well as *XMM/Newton* and *Chandra* Plionis et al. (e.g. 2005). Unfortunately, most of the serendipitous cluster observations are of relatively poor clusters, which are much more numerous. A targeted campaign of a representative sample of maxBCG clusters that have not previously been known to be X-ray bright will be essential to both test our measurement of the scatter in $L_X-N_{200}$ and to estimate the fraction of cluster flux that is contaminated by point sources. This will be essential to enable future inexpensive deep optical cluster surveys such as DES (Abbot et al. 2005) to use optical properties of clusters to estimate which clusters would be most useful to follow-up with targeted X-ray observations.

## REFERENCES

Abbot, T., et al. 2005, ArXiv Astrophysics e-prints, astro-ph/0510346

Abell, G. O. 1958, ApJS, 3, 211

Abell, G. O., Corwin, Jr., H. G., & Olowin, R. P. 1989, ApJS, 70, 1

Adelman-McCarthy, J. K., & et al. 2007, VizieR Online Data Catalog, 2276, 0

Allen, S. W. 1998, MNRAS, 296, 392

Anders, E., & Grevesse, N. 1989, Geochim. Cosmochim. Acta, 53, 197

Andersson, K. E., & Madejski, G. M. 2004, ApJ, 607, 190

Arnaud, K. A. 1996, in Astronomical Society of the Pacific Conference Series, Vol. 101, Astronomical Data Analysis Software and Systems V, ed. G. H. Jacoby & J. Barnes, 17–+

Bahcall, N. A. 1977, ApJ, 217, L77

Bardeau, S., Soucail, G., Kneib, J.-P., Czoske, O., Ebeling, H., Hudelot, P., Smail, I., & Smith, G. P. 2007, A&A, 470, 449

Basilakos, S., Plionis, M., Georgakakis, A., Georgantopoulos, I., Gaga, T., Kolokotronis, V., & Stewart, G. C. 2004, MNRAS, 351, 989

Bauer, F. E., Fabian, A. C., Sanders, J. S., Allen, S. W., & Johnstone, R. M. 2005, MNRAS, 359, 1481

Becker, M. R. et al. 2007, ArXiv e-prints, 704, 0704.3614

Biviano, A. 2000, in Constructing the Universe with Clusters of Galaxies

Biviano, A., Murante, G., Borgani, S., Diaferio, A., Dolag, K., & Girardi, M. 2006, A&A, 456, 23

Böhringer, H., Burwitz, V., Zhang, Y.-Y., Schuecker, P., & Nowak, N. 2005, ApJ, 633, 148

Böhringer, H. et al. 2004, A&A, 425, 367

—. 2000, ApJS, 129, 435

Borgani, S. 2003, Memorie della Societa Astronomica Italiana Supplement, 3, 209

Bower, R. G., Bohringer, H., Briel, U. G., Ellis, R. S., Castander, F. J., & Couch, W. J. 1994, MNRAS, 268, 345

Bower, R. G., Castander, F. J., Ellis, R. S., Couch, W. J., & Boehringer, H. 1997, MNRAS, 291, 353

Burenin, R. A., Vikhlinin, A., Hornstrup, A., Ebeling, H., Quintana, H., & Mescheryakov, A. 2006, ArXiv Astrophysics e-prints, astro-ph/0610739

Chen, Y., Reiprich, T. H., Böhringer, H., Ikebe, Y., & Zhang, Y.-Y. 2007, A&A, 466, 805

Colless, M. et al. 2001, MNRAS, 328, 1039

Collins, C. A., Guzzo, L., Nichol, R. C., & Lumsden, S. L. 1995, MNRAS, 274, 1071

Conroy, C., Wechsler, R. H., & Kravtsov, A. V. 2006, ApJ, 647, 201

Croft, S., de Vries, W., & Becker, R. H. 2007, ArXiv e-prints, 0708.0585

Croton, D. J., Gao, L., & White, S. D. M. 2007, MNRAS, 374, 1303

Cypriano, E. S., Sodré, L. J., Kneib, J.-P., & Campusano, L. E. 2004, ApJ, 613, 95

Dahle, H., Kaiser, N., Irgens, R. J., Lilje, P. B., & Maddox, S. J. 2002, ApJS, 139, 313

Dai, X., Kochanek, C. S., & Morgan, N. D. 2007, ApJ, 658, 917

De Filippis, E., Sereno, M., Bautz, M. W., & Longo, G. 2005, ApJ, 625, 108

Dickey, J. M., & Lockman, F. J. 1990, ARA&A, 28, 215

Donahue, M. et al. 2001, ApJ, 552, L93

—. 2002, ApJ, 569, 689

Ebeling, H., Edge, A. C., Bohringer, H., Allen, S. W., Crawford, C. S., Fabian, A. C., Voges, W., & Huchra, J. P. 1998, MNRAS, 301, 881

Ebeling, H., Voges, W., Bohringer, H., Edge, A. C., Huchra, J. P., & Briel, U. G. 1996, MNRAS, 281, 799

Edge, A. C., & Stewart, G. C. 1991, MNRAS, 252, 428

Edge, A. C., Stewart, G. C., Fabian, A. C., & Arnaud, K. A. 1990, MNRAS, 245, 559

Eisenstein, D. J. et al. 2001, AJ, 122, 2267

Fischer, P. 1999, AJ, 117, 2024

Fukugita, M., Ichikawa, T., Gunn, J. E., Doi, M., Shimasaku, K., & Schneider, D. P. 1996, AJ, 111, 1748

Gal, R. R. 2006, ArXiv Astrophysics e-prints, astro-ph/0601195

Gilbank, D. G., Bower, R. G., Castander, F. J., & Ziegler, B. L. 2004, MNRAS, 348, 551

Gioia, I. M., & Luppino, G. A. 1994, ApJS, 94, 583

Gunn, J. E. et al. 1998, AJ, 116, 3040

Gursky, H., Kellogg, E., Murray, S., Leong, C., Tananbaum, H., & Giacconi, R. 1971, ApJ, 167, L81+

Hansen, S. M., McKay, T. A., Wechsler, R. H., Annis, J., Sheldon, E. S., & Kimball, A. 2005, ApJ, 633, 122

Helsdon, S. F., & Ponman, T. J. 2000, MNRAS, 315, 356

Hilton, M. et al. 2005, MNRAS, 363, 661

Hoekstra, H. 2007, ArXiv e-prints, 705, 0705.0358

Horner, D. J., Mushotzky, R. F., & Scharf, C. A. 1999, ApJ, 520, 78

Johnston, D., et al. 2007, in preparation

Kaiser, N. 1986, MNRAS, 222, 323

Kelly, B. C. 2007, ArXiv e-prints, 0705.2774

Kochanek, C. S., White, M., Huchra, J., Macri, L., Jarrett, T. H., Schneider, S. E., & Mader, J. 2003, ApJ, 585, 161

Koester, B. P. et al. 2007a, ApJ, 660, 239

—. 2007b, ApJ, 660, 221

Kravtsov, A. V., Vikhlinin, A., & Nagai, D. 2006, ApJ, 650, 128

LaRoque, S. J., Bonamente, M., Carlstrom, J. E., Joy, M. K., Nagai, D., Reese, E. D., & Dawson, K. S. 2006, ApJ, 652, 917

Ledlow, M. J., Voges, W., Owen, F. N., & Burns, J. O. 2003, AJ, 126, 2740

Lin, Y.-T., & Mohr, J. J. 2004, ApJ, 617, 879

Mahdavi, A., Finoguenov, A., Böhringer, H., Geller, M. J., & Henry, J. P. 2005, ApJ, 622, 187

Mahdavi, A., Hoekstra, H., Babul, A., Sievers, J., Myers, S. T., & Henry, J. P. 2007, ArXiv Astrophysics e-prints, astro-ph/0703372

Markevitch, M. 1998, ApJ, 504, 27

Martini, P., Mulchaey, J. S., & Kelson, D. D. 2007, ArXiv e-prints, 0704.3455

Maughan, B. J. 2007, ArXiv Astrophysics e-prints, astro-ph/0703504

Mohr, J. J., Mathiesen, B., & Evrard, A. E. 1999, ApJ, 517, 627

Morrison, G. E., Owen, F. N., Ledlow, M. J., Keel, W. C., Hill, J. M., Voges, W., & Herter, T. 2003, ApJS, 146, 267

Mulchaey, J. S., Davis, D. S., Mushotzky, R. F., & Burstein, D. 2003, ApJS, 145, 39

Mullis, C. R. et al. 2003, ApJ, 594, 154

Nagai, D. 2006, ApJ, 650, 538

Nagai, D., & Kravtsov, A. V. 2005, ApJ, 618, 557

Neumann, D. M., & Arnaud, M. 1999, A&A, 348, 711

Nord, B., Stanek, R., Rasia, E., & Evrard, A. E. 2007, ArXiv e-prints, 0706.2189

O'Hara, T. B., Mohr, J. J., Bialek, J. J., & Evrard, A. E. 2006, ApJ, 639, 64

Ortiz-Gil, A., Guzzo, L., Schuecker, P., Böhringer, H., & Collins, C. A. 2004, MNRAS, 348, 325

Peres, C. B., Fabian, A. C., Edge, A. C., Allen, S. W., Johnstone, R. M., & White, D. A. 1998, MNRAS, 298, 416

Pfeffermann, E. et al. 1987, in Presented at the Society of Photo-Optical Instrumentation Engineers (SPIE) Conference, Vol. 733, Soft X-ray optics and technology; Proceedings of the Meeting, Berlin, Federal Republic of Germany, Dec. 8-11, 1986, Bellingham, WA, Society of Photo-Optical Instrumentation Engineers, Volume 733, 1987, p. 519., ed. E.-E. Koch & G. Schmahl, 519–+

Plionis, M., Basilakos, S., Georgantopoulos, I., & Georgakakis, A. 2005, ApJ, 622, L17

Popesso, P., Biviano, A., Böhringer, H., & Romaniello, M. 2007, A&A, 461, 397

Popesso, P., Böhringer, H., Brinkmann, J., Voges, W., & York, D. G. 2004, A&A, 423, 449

Rasia, E., Mazzotta, P., Borgani, S., Moscardini, L., Dolag, K., Tormen, G., Diaferio, A., & Murante, G. 2005, ApJ, 618, L1

Raymond, J. C., & Smith, B. W. 1977, ApJS, 35, 419

Romer, A. K. et al. 2000, ApJS, 126, 209

Rosati, P., della Ceca, R., Norman, C., & Giacconi, R. 1998, ApJ, 492, L21+

Rozo, E. et al. 2007a, ArXiv Astrophysics e-prints, astro-ph/0703571

—. 2007b, ArXiv Astrophysics e-prints, astro-ph/0703571

Rykoff, E. S., et al. 2007, in preparation

Sanderson, A. J. R., Ponman, T. J., Finoguenov, A., Lloyd-Davies, E. J., & Markevitch, M. 2003, MNRAS, 340, 989

Sheldon, E. S., et al. 2007, submitted

Smail, I., Edge, A. C., Ellis, R. S., & Blandford, R. D. 1998, MNRAS, 293, 124

Smith, J. A. et al. 2002, AJ, 123, 2121

Squires, G., Kaiser, N., Babul, A., Fahlman, G., Woods, D., Neumann, D. M., & Boehringer, H. 1996, ApJ, 461, 572

Stanek, R., Evrard, A. E., Böhringer, H., Schuecker, P., & Nord, B. 2006, ApJ, 648, 956

Strauss, M. A. et al. 2002, AJ, 124, 1810

Voges, W. et al. 1999, A&A, 349, 389

—. 2000, VizieR Online Data Catalog, 9029, 0

Voges, W., Boller, T., Englhauser, J., Freyberg, M., & Supper, R. 2001, in Astronomical Society of the Pacific Conference Series, Vol. 225, Virtual Observatories of the Future, ed. R. J. Brunner, S. G. Djorgovski, & A. S. Szalay, 234–+

Voit, G. M. 2005, Reviews of Modern Physics, 77, 207

Wechsler, R. H., Zentner, A. R., Bullock, J. S., Kravtsov, A. V., & Allgood, B. 2006, ApJ, 652, 71

White, N. E., Giommi, P., & Angelini, L. 2000, VizieR Online Data Catalog, 9031, 0

White, R. L., Becker, R. H., Helfand, D. J., & Gregg, M. D. 1997, ApJ, 475, 479

Xue, Y.-J., & Wu, X.-P. 2000, ApJ, 538, 65

Yee, H. K. C., & Ellingson, E. 2003, ApJ, 585, 215

Yee, H. K. C., & López-Cruz, O. 1999, AJ, 117, 1985

York, D. G. et al. 2000, AJ, 120, 1579

Zaroubi, S., Squires, G., de Gasperis, G., Evrard, A. E., Hoffman, Y., & Silk, J. 2001, ApJ, 561, 600

Zentner, A. R., Berlind, A. A., Bullock, J. S., Kravtsov, A. V., & Wechsler, R. H. 2005, ApJ, 624, 505

Zwicky, F. 1933, Helvetica Physica Acta, 6, 110

—. 1937, ApJ, 86, 217